crystals

MDPI

Article

Bio-Fabrication and Experimental Validation of an Mg - 25Ca - 5Zn Alloy Proposed for a Porous Metallic Scaffold

Luis Humberto Campos Becerra * and Alejandro Torres Castro *

Facultad de Ingeniería Mecánica y Eléctrica, Universidad Autónoma de Nuevo León (UANL), Pedro de Alba S/N, Ciudad Universitaria, San Nicolás de los Garza 66451, NL, Mexico

* Correspondence: luis.camposbcr@uanl.edu.mx (L.H.C.B.); alejandro.torrescs@uanl.edu.mx (A.T.C.); Tel.: +52-(392)100-12-00 (L.H.C.B.)

Abstract: This paper proposes the bio-fabrication of a porous scaffold from a selection procedure of elements taking into account biological behavior, using magnesium (Mg) alloyed with calcium (Ca) and zinc (Zn). The proposed scaffold could work as a treatment for specific pathologies in trauma and oncology, on the one hand, in addition to possible applications in osteosynthesis, through contrib-uting to osseointegration and infection control through the release of drugs. Finally, another pos-sible attribute of this alloy could be its use as a complementary treatment for osteosarcoma; this is due to the basification produced by oxidative degradation (attack on cancer cells). The evaluation of cell viability of an alloy of Mg - 25 wt% Ca - 5 wt% Zn will strengthen current perspectives on the use of Mg in the clinical evaluation of various treatments in trauma and oncology. Considera-tions on the preparation of an alloy of Mg - 25 wt% Ca - 5 wt% Zn and its morphological charac-terization will help researchers understand its applicability for the development of new surgical techniques and lead to a deeper investigation of alternative treatments. However, it is very im-portant to bear in mind the mechanical effect of elements such as Ca and Zn on the degradation of the alloy matrix; the best alternative to predict the biological-mechanical potential starts with the selection of the essential-nutritional elements and their mechanical evaluation by mi-cro-indentation due to the fragility of the matrix. Therefore, the morphological evaluation of the specimens of Mg - 25 wt% Ca - 5 wt% Zn will show the crystallinity of the alloy; these results to-gether contribute to the design of biomedical alloys for use in treatments for various medical spe-cialties. The results indicated that cell viability is not affected, and there are no morphological changes in the cells.

Keywords: porous magnesium scaffold; casting of Mg base alloys; morphological characterization; cell viability; micro-indentation; toxicity

Citation: Becerra, L.H.C.; Castro, A.T. Bio-Fabrication and Experimental Validation of an Mg - 25Ca - 5Zn Alloy Proposed for a Porous Metallic Scaffold. *Crystals* **2021**, *11*, 1416. https://doi.org/10.3390/cryst11111416

Academic Editors: Hanuma Reddy Tiyyagura, Yasir Beeran Pottathara, Pavel Lukáč, Mantravadi Krishna Mohan and Srinivasan Arthanari

Received: 12 October 2021
Accepted: 14 November 2021
Published: 19 November 2021

1. Introduction

Currently, the use of biomaterials in various applications such as orthognathic surgery has driven the development of techniques using allografts, autologous implants and demineralized bone matrix (DBM), However, according to the American Association of Tissue Banks (AATB), deregulation has led to problems, because bone must be harvested from the patient and/or corpse, causing risks of infections, morbidity and potential legal issues [1–6]. A base biomaterial Mg - 25 wt% Ca - 5 wt% Zn that can be used as a scaffold for the fractured bone to recover, avoiding tissue laceration and re-operation, can provide a higher healing rate without the risks associated with the primary procedure [7–10]. For applications where a scaffold is required as a complement to manage a fracture, the proposal of a porous scaffold made of Mg - 25 wt% Ca - 5 wt% Zn has become an interesting option [10–12], because the FDA has determined that the products contained within a human demineralized bone matrix (DBM), do not comply with the provisions of Section 361 of the public health service law, mainly because they are not sterilizing agents [13]. Other options such as synthetic bone graft extenders have properties similar

to cadaver bone, however they do not contain the necessary products to stimulate bone regeneration [12,14,15]. The release of Mg ions in vivo are conducive to an accumulation of the element around the fracture sites, favoring the formation of cortical bone [16,17]. Another option is to use the bone morphogenetic protein, BMP-2, which has been shown to induce osteogenesis through cellular alteration, producing fibrous tissue. Several authors have proposed using elements such as Ca and Zn to improve the behavior of Mg in vivo; nutritional and essential elements for the body should be the first option in optimizing Mg for biomedical purposes [10,18–27]. This article intends to contribute conclusions to the ISO/TC 194/WG5 committee, on the results of cell viability for Mg - 25 wt% Ca - 5 wt% Zn alloys, due to the acceptable levels shown under the ISO-10993 evaluation [28,29]. There are currently organizations that have results from technovigilance programs that show favorable results for manufacturing medical devices from these alloys [20,30]. The objective of the study is the evaluation of the biological and structural effect of the addition of Zn on a MgCa master alloy and to verify that an alloy can be biologically designed from the selection of its elements. The research is intended as a contribution toward a possible biomedical application on the effect of Zn on crystallization in MgCa. Figure 1 shows the combination of a straight CMF plate (craniomaxillofacial) and a proposed Mg-based porous scaffold for the reconstruction and lengthening of the mandibular body.

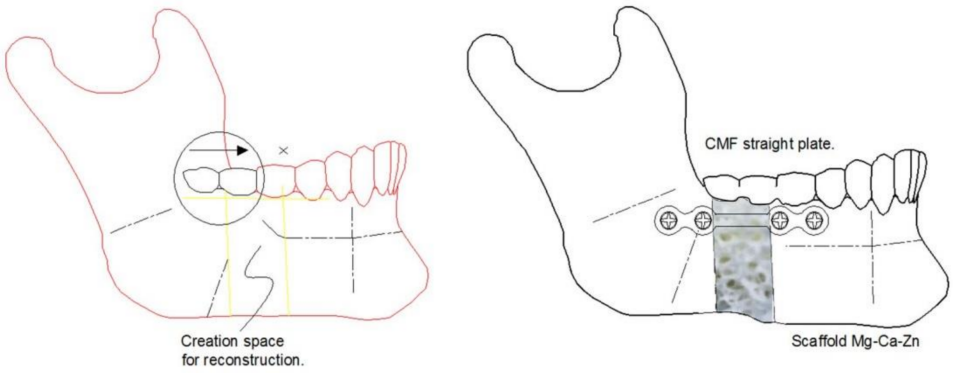

Figure 1. Lengthening of the mandibular body.

Designing a biomedical Mg - 25 wt% Ca - 5 wt% Zn alloy with a degradable matrix and zero toxicity poses challenges and opportunities; in particular mechanical resistance is a factor that must be resolved [31]. However, toxicity is a fundamental aspect of the problem and must be taken into account in the design stages. Furthermore, the mole fraction ratio of the elements and their solubility limits are important in understanding the mechanisms of grain growth and second phase formation [32–34]; the alloy must withstand the biomechanical loads of the body for pathologies where a BDM scaffold is required [35,36]. Senkov et al. reported in their study that Ca, Mg and Zn provide the highest packing efficiency of the amorphous state [37]. Taking care of the percentages of elements in the formulation of an alloy and relating it to degradation will offer benefits on the toxicological impact of the alloy, which can be verified in in vitro experimentation on the cell viability of the alloy [38]. For this reason, keeping in mind the daily intake limits for each element is essential to promote biocompatibility in this type of alloy.

In the smelting of non-ferrous alloys, oxidation should be avoided. It is advisable to melt in a reductive atmosphere using gases such as argon, SF6 and/or Flux; in addition, using a vacuum will reduce porosity and generate grain refining [6,39–41]. The diffusion-controlled oxidation process obeys the parabolic law [41,42].

Micro-indentation techniques have allowed the analysis of data such as force-displacement from small volumes of material, from which the elastic modulus and hardness can be obtained; this application has allowed experimentation in trabecular, Ostional and lamellar bone. With this technique, it is possible to explore the anisotropic elastic behavior of materials with lamellar formation, such as in the case of the Mg - 25 wt% Ca - 5 wt% Zn

alloy, where the $MgCa_2$ phase has a lamellar-eutectic behavior. Moreover, with these data it will be possible to understand in greater depth the theoretical development of fracture mechanisms [43–46]. A Mg - 25 wt% Ca - 5 wt% Zn-based biomaterial that is used in the manufacture of a clinical implant will exhibit brittle behavior, which implies that failures will occur due to exposure to cyclical loads due to fatigue. However, due to Mg, this problem worsens, so identifying the morphology will serve as an initial effort to identify strategies that mitigate degradation [24].

Mg as an element in an alloy contributes by inducing an anti-vibratory effect. For biomedical applications, this is an excellent attribute due to its ability to absorb kinetic and potential energy, which may be a unique feature that helps counteract the shear loads that produce bone neo-formation [47].

Lui et al. developed a histological evaluation on Mg-Zn and observed the formation of new trabeculae surrounded by osteoblasts and osteoclasts; consequently, they observed mature bone tissue and lamellar bone, as characteristics fundamental for the consolidation of bone regeneration [48,49]. Chang et al. carried out a histological study in animals, observing good tolerance of the organism to metal ions, showing from an early stage a biocompatible response [50]. Sarkar et al. report proliferation of osteocytes and mononuclear cells in the medullary cavity of a rabbit femur, indicating the beginning of an important healing process from Zn-doped MgP [51,52].

2. Materials

An alloy of Mg - 25 wt% Ca - 5 wt% Zn of biological inspiration was formulated. Given the behavior of Mg, the alloy will be degradable in vivo in approximately 150 days. Considering the toxicological limits of Ca and Zn, which are considered nutritional and essential elements, these elements are normally found in the form of ions in the human body, while Zn frequently comes from the diet [22,53,54].

For the design of this alloy, it was proposed to use 69.18% Mg, 25.82% Ca and 4.99% Zn, considering a final weight for a device of 30 g, which corresponds to 20.75 g Mg, 7.74 g Ca and 1.49 g of Zn. If a linear degradation at 150 days is assumed and the permitted value in g/day for the human body is considered, these percentage and gram quantities for an alloy would not represent a toxicological risk for the organism. When using these percentages for the design of an alloy, the allowed value for these elements is not exceeded; Mg, Ca and Zn respectively show 0.14, 0.052 and 0.010 g/day, these values being well below the toxicological limit. See Table 1.

This formulation is valid for class III implants or medical devices, weighing $\leq$ 30 g. Due to the risk associated with the use of Zn, the ideal weight proposed for the implant made from this alloy is 30 g. Raising the weight in g could cause an increase in the Zn content; thus, this development proposes keeping the Zn to a lower percentage. The following criterion was used, not to exceed 60% of the toxicological limit of Zn, which leaves us a value of 0.010 g/day. It should be considered that the average nutritional diet of people can enrich the content of this element in the body and for this reason a low Zn diet is recommended while the patient recovers from the surgical procedure.

Table 1. Alloy design based on toxicological limit and biodegradation.

%	Element	Degradation Days	Weight in g.	Complies for Toxicology g/Days	Toxicological Limit in g/Days
69.18	Mg	150	20.75	0.140	0.700
4.99	Zn	150	1.49	0.010	0.015
25.83	Ca	150	7.74	0.052	0.800

In the biofabrication of this alloy, an induction furnace TF4000 (INDUTHERM, Erwärmungsanlagen GmbH, Germany) was used; conditions such as the heating ramp were determined from a series of experiments shown in Figure 2, in foundry 1 and 2 and the alloy was not homogenized, initiating an ignition process due to the high temperature, which

was mainly attributed to the absence of the argon protective atmosphere during preheating and the casting process. Mg reactivity limits its use [30]. The use of Flux (Melrasal) and the Ar atmosphere were the positive differences in casting 3. In addition, the temperature and time parameters were adjusted, as shown in the curve. The homogenization period that allowed an adequate diffusion of the Zn powder on the MgCa master alloy corresponds to 36 min.

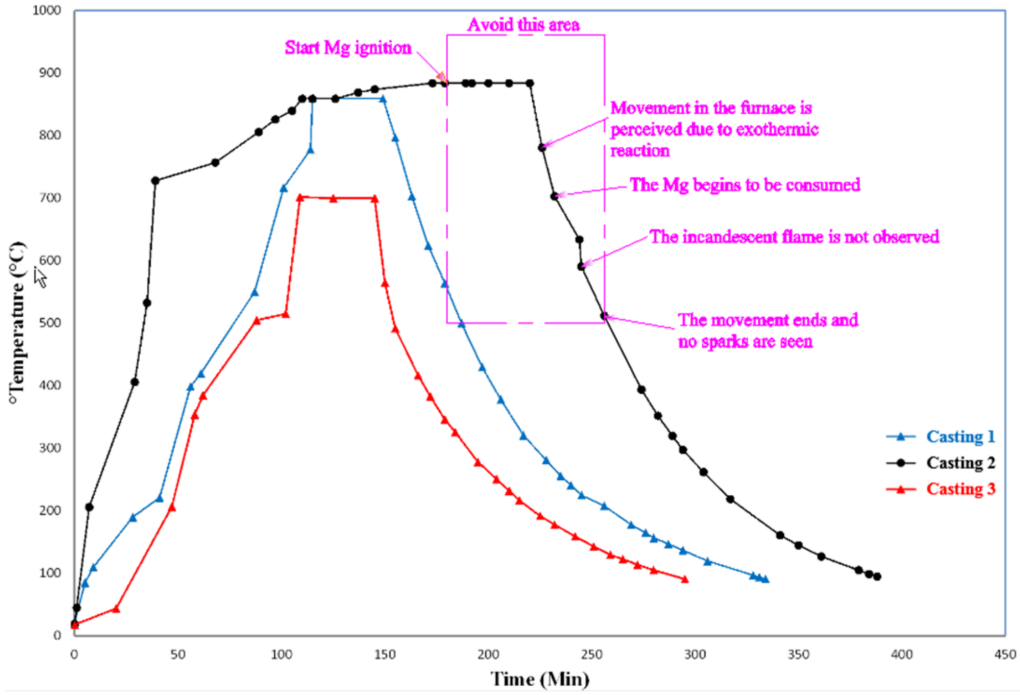

Figure 2. Casting 3; heating ramp 6.42 °C min^{-1}, homogenization 36 min-700 °C, cooling ramp 4.06 °C min^{-1}.

The induction smelting process followed the preheating of the smelting system to avoid humidity, inducing a reductive atmosphere of Argon (99,999) used to purge the interior of the Mg oxide crucible. Prior to purging with argon, a second 244 mL 80 × 63 mm porcelain crucible with a lid was placed inside the Mg oxide crucible containing the charge of the elements Mg - 30 wt% Ca master alloy (purified Zn, Fremont, CA, USA); these were completely covered with Flux (Melrasal UE, Magnesium elektron, Manchester, UK). A flow of Argon (5×10^{-2} torr) was kept constant from the preheating process of the furnace until the porcelain crucible was extracted when cooling.

During the smelting process, using argon reduces evaporation. It is necessary to have a gas purification system which will reduce contraction; to homogenize the casting, the temperature was maintained for 36 min at 700 °C. rapid solidification is recommended to increase strength and elongation and improve processability, this will allow an abrupt and ideal transition to cooling to form a smaller grain [37]. The density of the alloy was calculated from the chemical composition and corresponds to 1.9534 kg/m^3. Kumar et al. reported that the limitations of Mg smelting are characterized by a precarious distribution of elements causing segregation and porosity [43]. Avoiding the contact of the elements to be melted with other surfaces is of vital importance to avoid contamination with traces and impurities [39].

In the previously proposed formulation Mg - 25 wt% Ca - 5 wt% Zn, it is considered that increasing the Zn content by more than 1 wt% will reduce the amount of hydrogen formed in the reaction, Mg (s) + $2H_2O \rightarrow Mg(OH)_2$ (aq) + H_2 (g), which contributes to improving the corrosion rate [55,56]. Exceeding the percentage of Zn by 5 wt% in the suggested chemical composition will increase the cytotoxic level, which will reduce cell

viability. This alloy exhibits brittle behavior for which cold deformation treatments such as ECAP are suggested to increase its strength. Vinogradov et al. presented a study where severe plastic deformation refined the microstructure and produced a modification on the surface texture of Mg, improving the resistance [57–62]. Afandy et al. has reported that some mechanical treatments can nano-structure the surface of materials [63]. Thermal stability depends on microstructural parameters, such as the composition of the phases [64]. One of the biggest unknowns to date is the toxicological impact in vivo due to the size of a nanoparticle on the evolution of the pathophysiology reported for different chemical elements. This shows a causal relationship between the quantity of elements and the release of nanoparticles to the organism.

Special care must be taken with heat treatments as these affect the corrosion rate, due to the fact that intermetallic phases resulting from casting may dissolve. The weakening and random basal texture can be obtained after the annealing [65]. Adding 1 wt% in Ca increases the tensile strength; the solubility of Ca in Mg is 1.34% wt at 789 °K. The incorporation of Ca and Zn on Mg helps increase the mechanical properties [19,22,66–80]. Sergio Medina et al. present information on the complexity of strengthening MgCa alloys by heat treatment. Adding Ca reduces the ignition point of Mg, however the hardness decreases when it exceeds 1.8 wt% [19,81]. Figure 3 shows the result of the third casting test of the alloy Mg - 25 wt% Ca - 5 wt% Zn.

Figure 3. Mg - 25 wt% Ca - 5 wt% Zn.

This figure shows Mg base alloy Mg - 25 wt% Ca - 5 wt% Zn (Magnesium: 63.19 wt%: Calcium: 25.03 wt%: Zinc: 5.18 wt%: Oxygen: 6.60 wt%). Obtained by atomic diffusion of Zn over MgCa, it is proposed for the manufacture of a porous scaffold, which must have mechanical and biological properties like DBM to be used as an alternative in orthognathic or related pathologies. The validation of cell viability and its mechanical properties, obtained under micro-indentation and techniques such as SEM-EDS, TEM and XRD, must comply with what is related to ISO10993, leading to a viable proposal. The behavior of the material is fragile due to the secondary phases and its lamellar morphology [82]. Senkov et al. reported in their study that the $CaMg_2$ phase has slow nucleation kinetics [37]. Jardim et al., reported that this $CaMg_2$ phase has a high melting point and is characterized by an adequate intermetallic balance [83].

3. Methods

Several techniques such as SEM-EDS, XRD, TEM, micro-indentation and cell viability were combined to explain, through a combinatorial approach, the properties and behavior of the proposed alloy for a porous scaffold. The composition and formation of the phases originate the mechanical behavior, while the detachment of the constituents from the alloy matrix modifies the biological behavior, depending on the concentration and release rate. Having the information on the performance of the proposed alloy can help to understand its applicability in different pathologies as an alternative biomaterial. The use of Mg alloys has been suggested in applications where the load applied to the bone structure is minimal or very low; therefore, applications in orthognathic surgery are a field of development for these materials [39].

3.1. SEM-EDS

The metallographic samples were roughened with 300–3000 sandpaper and polished with 0.3 µm alumina paste. In the microscope configuration, the filament and the current emission window were checked, the intensity was confirmed at 2, the sample was inserted into the holder and was is carried out. The microscope was equipped with an energy dispersive spectrometer (EDS) to obtain the distribution of the elements in the microregions of interest and thus be able to confirm the diffusion. A metallographic preparation was performed on a specimen by performing a microscopy utilizing scanning electron microscopy-energy dispersive X-ray spectroscopy (SEM-EDS). To reveal the morphology of the Mg - 25 wt% Ca - 5 wt% Zn alloy, it was performed with a microscope, Nanosem200-FEI, (Netherlands), sticking the samples to a sample holder with a graphite tape. The micrograph and the analysis employing EDS were obtained in an atmosphere under vacuum, and magnifications were obtained with a resolution of 10 µm. SEM-EDS analysis used configuration parameters that correspond to 20 KeV at a magnification of 1469.

3.2. XRD

The morphology of samples was characterized by X-ray diffraction (XRD). XRD results showed the formation of biocompatible phases of $MgCa_2$ and magnesium oxide on the surface of alloy Mg - 25 wt% Ca - 5 wt% Zn. In their work, Sourav Dutta et al. work show how the degradation of implants manufactured in Mg produces the release of Mg oxide. In addition they presented how this compound is used by the human body in the recovery of bone fractures [84]. X-ray diffraction analysis (XRD), by means of an equipment empyrean, (Spain) was used to evaluate the present phases of the Mg - 25 wt% Ca - 5 wt% Zn alloy. The XRD analysis was acquired from 5–130° with a step size of 0.03 at 40 mA and 45 keV using Cu Kα radiation.

3.3. TEM-FIB

A lamella was prepared for TEM. Through a focused ion beam (FIB) thinning from gallium to approximately 60 nm, with a double beam system, (FEI QUANTA 200 3D, The Netherlands), it was mounted on a grid keeping it under vacuum even before observation. The lamella was placed in a holder inside the equipment (TEM, Titan 80–300-FEI, The Netherlands) (Figure 6). Gallium is a beneficial element in osteosynthesis: it inhibits bone resorption [85]. The TEM operating conditions correspond to 300 keV and 380 magnification, with an aperture for condenser lens # 2 of 150, the exposure time corresponds to 1 s. In Figure 7 the diffraction pattern of the Mg - 25 wt% Ca - 5 wt% Zn alloy is shown, in high vacuum conditions from 10^4 to 10^7, to achieve an uninterrupted flow of electrons, the images that are observed correspond to the diffraction of the selected area of the lamella, this corresponds to bright field and dark field. The FIB thinning technique aims to highlight the nano-structure and crystallography of metallic products of Mg [86].

The identification of the planes was carried out with the help of the list of indexed peaks of the diffraction charts of the International Center for Diffraction Data (ICDD). This was done for each phase by relating the interplanar measurement of TEM, looking for a coincidence with respect to 2 theta in the list of indexed peaks. and thus relating it to the hkl planes.

3.4. Micro-Indentation

Specimens for micro-indentation were previously prepared, polished, and mounted on a holder which had holes to allow its holding. The tests were carried out at room temperature: two small sections were analyzed longitudinally and transversely, and both samples were embedded in a resin epoxy without use of vacuum. After being ground using abrasive papers of decreasing grit size (300, 800 and 3000 grit) under deionized water, with successively finer grades of alumina powder, the finest being 0.3 µm the specimens were cleaned ultrasonically to remove surface debris.

The micro-indentation cycle consists of adequately focusing the sample surface, adjusting the load-displacement, stabilizing the system, unloading on the sample, maintaining the load for a relatively longer time, which allowed the thermal derivative to be calculated and finally completing the download. This test was performed with a Berkovich type indenter.

Experiments described here were conducted using a nanoindenter 50-00191 NHTX S/N (CSM instruments). The system made small marks in precise positions on a sample surface and acquired the load-displacement of the diamond indenter using the Oliver and Pharr method, using parameters such as approach speed 6000 nm/min, delta slope contact 80%, acquisition rate 10 Hz, max load 20 mN, loading-unloading rate 200 mN/min, pause 1 s and poisson ratio 0.30. The samples were kept positioned in an x-y-z triad system relative to the microscope. The instrument is insulated in a cabin to allow thermal stability and suspended on a pneumatic anti-vibration table to protect the results from external vibrations.

3.5. Cell Viability

Specimens were machined into small 3 × 3 × 15 mm bars to perform a cell viability evaluation, through which we sought to represent the morphological changes. All procedures were carried out under aseptic conditions and in a sterile environment, ensuring cell recovery, adherence, and progression towards the exponential growth phase [87]. Extracts were obtained by the elution method according to ISO 10993-12. Samples of Mg - 25Ca - 5Zn were immersed in the cell culture medium for 24 h at 5% CO_2, 95% humidity and 37 °C, with a fixed ratio of surface area to medium volume of 1.25 cm^2/mL. [88] Then, extracts were collected and evaluated for impact on cell viability. Qing et al. have proposed using an indirect proliferation assay adapted from ISO-10993-5 [28]. Using an alloy of MgCa combined with collagen would improve bone regeneration, confirming the biological safety of the material [89]. The study presented corresponds to an evaluation of the cytotoxicity and cellular proliferation of L-929 cells. It is vitally important to avoid the concentration of Zn at a level of 80 µM, as it has been reported to inhibit cell viability and cell proliferation [90,91]. These previous findings correspond and agree with what was proposed in this work, defining a toxicological criterion for the use of Zn in Mg.

The murine fibroblast cell line (L-929; CCL1) was purchased from the American Type Culture Collection. Tissue culture medium, fetal bovine serum (FBS) and supplements were obtained from Gibco (IL, USA). Dyes, phosphate buffered saline (PBS) and dimethyl sulfoxide were purchased from Sigma-Aldrich Chemical Co (MO, USA). L-929 fibroblasts were grown in DMEM with 10% FBS and 2 mM L-glutamine in 5% CO_2, 95% humidity at 37 °C.

For the NRU method, cells were cultured in 96-well plates at a density of 1 × 10^5 cells/well and pre-cultured for 24 h to allow adaptation of the cells before adding the extracts. The five non-serial dilutions of extracts with culture media ranging from 10% to 100% were placed on cells in quadruplicate. The treatments with culture media were kept as a reference (100% viability). Zinc diethyldithiocarbamate (ZDC) 0.1% was used as a cytotoxic control.

After an incubation period of 48 h, the 96-well plate was centrifuged (210 g for 10 min) and the medium was replaced by the neutral red spot (100 µL of a 0.2 mg/mL cell culture medium) in each well and the plate. It was incubated again at 37 °C for 4 h. The plate was then washed with PBS once and then removed, allowed to dry for 1 h and 100 µL of neutral red eluent was added to each well. (Ethanol: dH2O: acetic acid 50:49:1). The plate was then shaken for 1 h to dissolve the dye. After the neutral red dissolved, the absorbance was measured spectrophotometrically using a microplate reader (xMark, BioRad, Louisville, KY USA) at a wavelength of 540 nm with a reference wavelength of 630 nm [29]. According to ISO 10993-5: 2009, a relative metabolic activity of less than 70% was considered cytotoxic.

Negative controls included treatments with culture media. The cytotoxicity of 0.1% zinc diethyldithiocarbamate (ZDC) in culture media was evaluated under the same experimental conditions as the positive control. The cell viability was estimated by measuring

the rate of mitochondrial reduction of tetrazolium-dye (MTT). The MTT assay determines the reduction of yellow soluble tetrazolium salt to an insoluble purple formazan crystal via a mitochondrial-dependent reaction only in metabolically active viable cells.

4. Results

The results obtained confirm the diffusion of Zn over the MgCa master alloy. Zn is not reflected in the composition of the distances that could be identified and measured, Zn could be phases due to inconsistencies in the sample and possibly the preferential orientation of the material. When mapping by EDS, interplanar location suggests that the part analyzed by XRD did not contain Zn, which is attributed to poor dispersion during solidificationl however, no change in cell viability was induced as a product of Zn. There are some peaks that could not be identified by means of XRD. When crossing the information with the observation by TEM, it is verified that there is Zn in the sample, which suggests the formation of tiny crystalline phases of $MgZn_2$.

4.1. SEM-EDS

The mapping of elements is shown in Figure 4 by means of a distribution analysis by SEM-EDS (O, Mg, Ca, and Zn). The main objective was the diffusion of Zn on the MgCa master alloy. There is a recrystallized microstructure with second phases in the matrix, without generalized homogenization due to the conditions of the casting process. In general there is no positive segregation of the elements; the diffusion of Zn on the MgCa master alloy is confirmed in the analysis by SEM-EDS. The lamellar morphology is very similar to that found in porous scaffolds for craniomaxillofacial reconstruction (CMF) [92]. Alshaaer et al. reported a pore size between 1–400 μm [4,6,10]. Mayama et al. reported that under compression conditions, porous Mg has a high energy absorption efficiency [10,93,94].

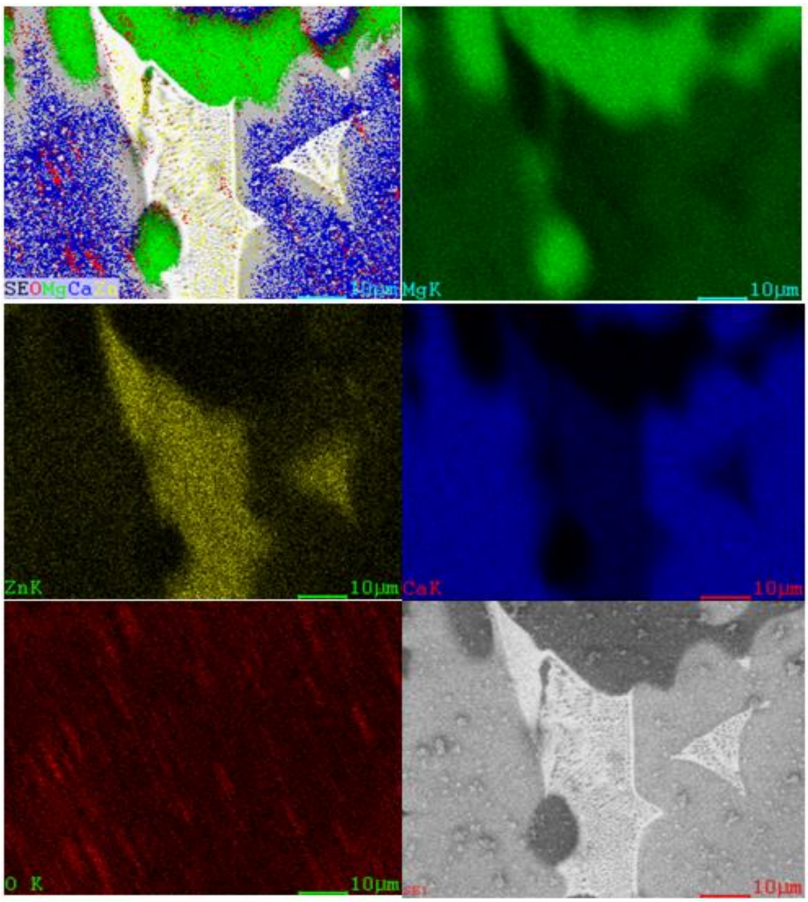

Figure 4. Element mapping by SEM-EDS (O, Mg, Ca, Zn) distribution of second phase particles.

4.2. XRD

Identification of secondary phases was carried out by XRD. This alloy is composed of microstructural phases α-Mg, $CaMg_2$ and MgO, presented as a periclass, a cubic form of Mg oxide. It was not possible to detect any phase as a product of Zn. Mguni et al. postulate in their experimentation that the periclass in the form of MgO detected by XRD crystallizes directly from nano-sheets [95–97]. The phases formed do not represent impurities that impair the cellular viability of the alloy [43].

Figure 5 shows the diffraction pattern and the identification of the $CaMg_2$ and α-Mg phases. Not all reflections agree with the $MgCa_2$ phase, presenting a strong preferential orientation in the plane (1 2 3) and confirming that there are reflections that do not coincide with any compound of Mg and Ca. The most intense reflections without coincidence are those of the angles 52.63 and 73.85 theta.

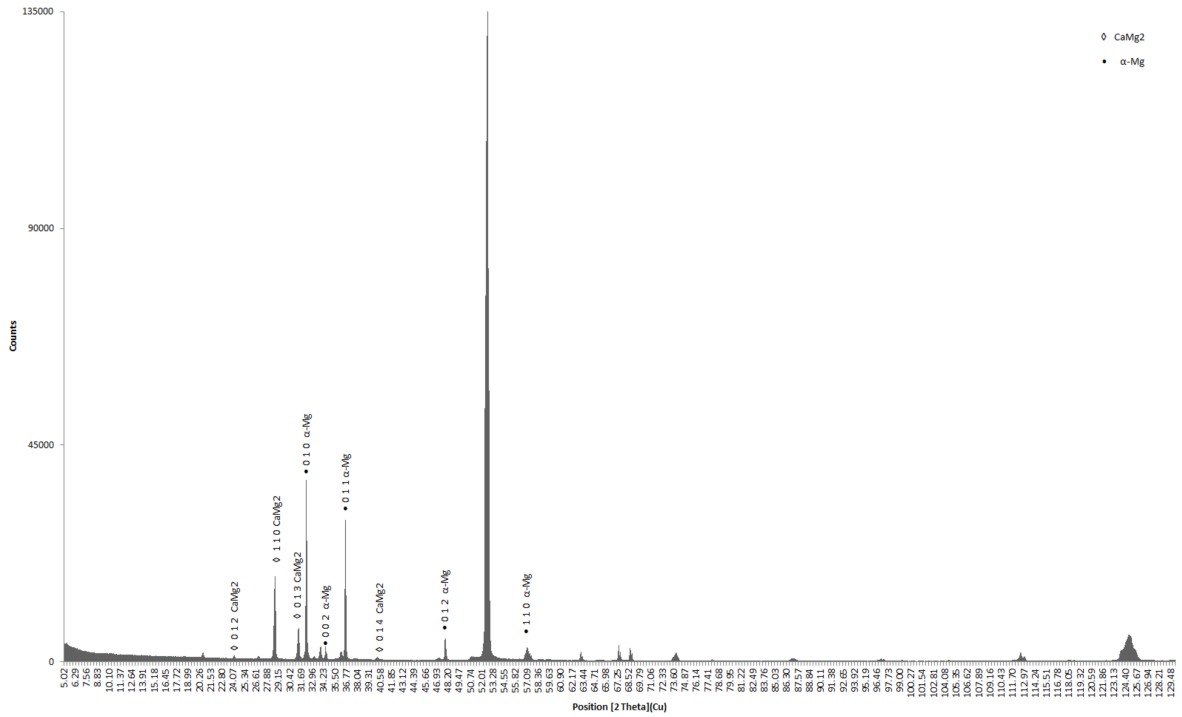

Figure 5. Diffraction pattern Mg - 25 wt% Ca - 5 wt% Zn.

Ramírez et al. reported a similar effect in a Mg-Zn-Al alloy. Although this may be due to the sensitivity limits of XRD, they reported a plane relationship to the MgO phase [6].

Zn is not present in the section of the sample analyzed by XRD diffraction, which could be due to the preferential orientation of the sample. Fuzeng Ren et al. reported in their work that the addition of Zn inhibits the crystallization of hydroxyapatite compounds [98]. Tripathy et al. presented evidence that solid solutions of Zn - Ca hydroxyapatite result in incoherent values in lattice constants and diffraction patterns [99,100]. There is a reduction in the degree of crystallization of the phases, increasing Zn and decreasing Ca in an Mg alloy will modify the network parameters a and c, which can be determined by the Rietveld refinement method.

4.3. TEM

Figure 6 shows bright field and dark field images obtained by TEM in addition to the FIB preparation of a lamella for observation by TEM. Figure 7 shows the linear measurement of the rings of the resulting diffraction pattern; two patterns are shown to highlight the identification of all the phases previously detected by XRD. With the ring measurement, it is directly related to the closest value corresponding to the interplanar

distance, d(A) of the diffraction charts, and indexing for each corresponding plane. This is shown for the α-Mg, $CaMg_2$ and MgO phases, respectively 01-1141, 13-0450 and 04-0829. Figures 8–10 show images of HRTEM and its interplanar measurement related to the phase diffraction plane.

Figure 8 shows HRTEM images, taken from the sites marked by A, B and C. Image A shows the measurement of the interplanar distance of the MgO phase, which corresponds to 2.106 Å in plane 2 0 0 at the 1 nm scale; the image was taken at 1.25 million magnification by the bright field technique. Image B shows the interplanar space d2 for the MgO phase and corresponds to 2.42 Å in the 1 1 1 plane. Image C shows the interplanar space 3 of the α-Mg phase Y, and corresponds to 2.60 Å in the plane 0 0 2.

Figure 9 displays HRTEM images, taken from the sites marked by A, B and C. Image A shows the measurement of the interplanar distance d6 of the α-Mg phase, which corresponds to 2.45 Å in the 1 0 1 plane, at the 1 nm scale. Image B shows the interplanar space d4 for the $CaMg_2$ phase and corresponds to 2.29 Å in the 1 0 4 planes. Image C shows the interplanar space d5 of the $CaMg_2$ phase and corresponds to 3.14 Å in the 1 1 0 plane.

Figure 10 shows HRTEM images, taken from the sites marked by A, B and C. Image A shows the measurement of the interplanar distance d7 of the $CaMg_2$ phase, which corresponds to 2.87 Å in the 1 0 3 planes, at the 1 nm scale. Image B shows the interplanar space d8 for the $CaMg_2$ phase and corresponds to 2.40 Å in the 2 0 2 planes. Image C shows the interplanar space d9 of the α-Mg phase and corresponds to 2.77 Å in the 1 0 0 plane.

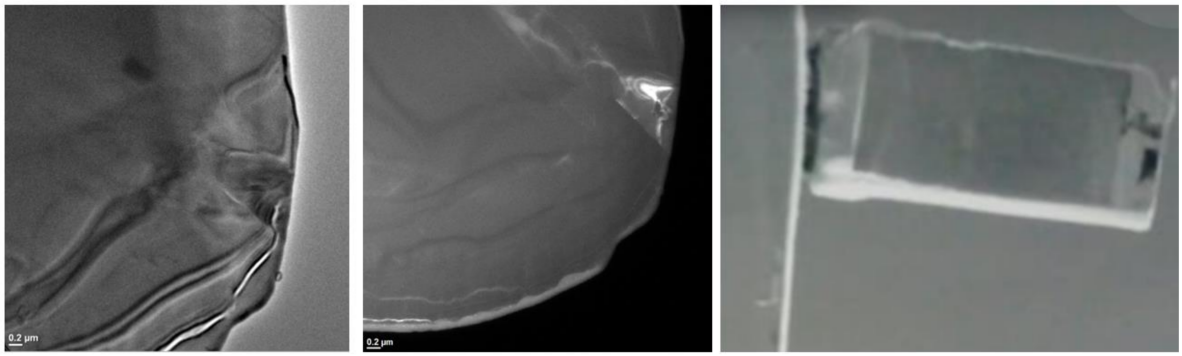

Figure 6. Bright field, dark field and preparation of lamella by focus ion beam (FIB).

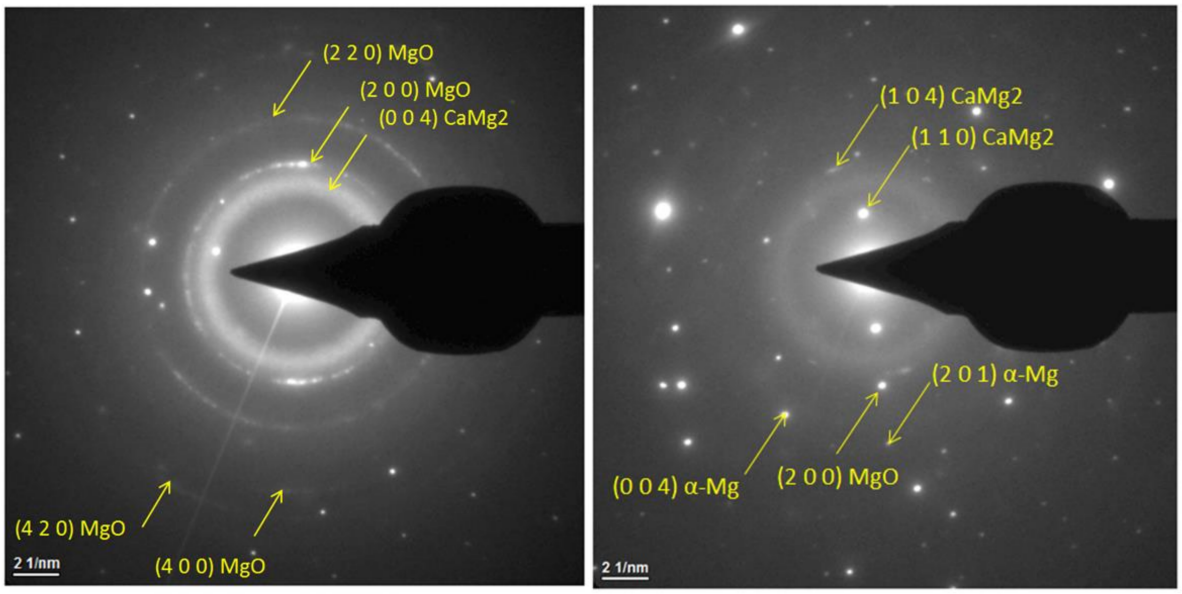

Figure 7. Diffraction patterns and identification to the α-Mg, $CaMg_2$ and MgO phases identified by XRD, referenced to diffraction charts of the International center for diffraction data (ICDD).

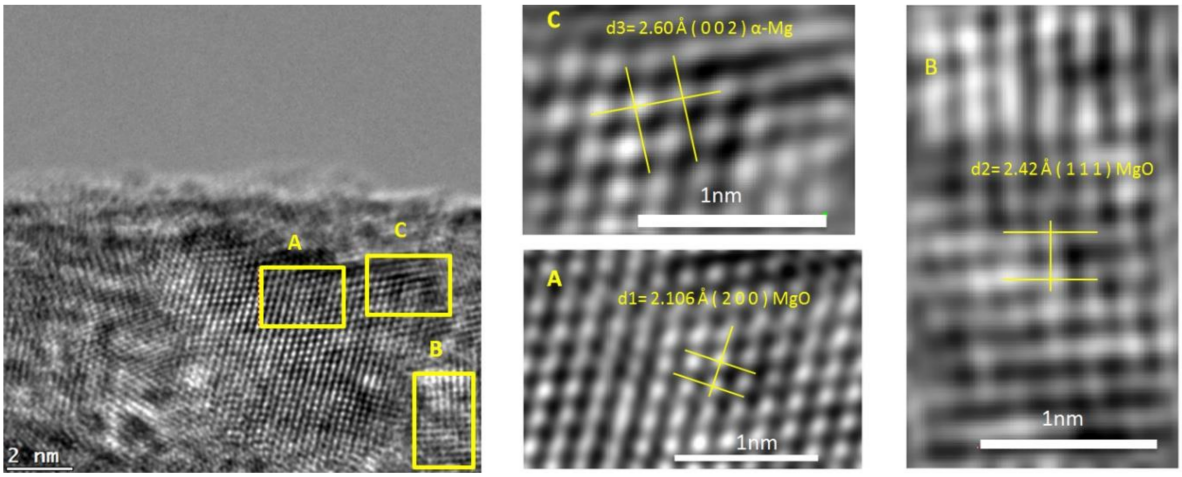

Figure 8. Plane identification with respect to interplanar space measurement on Mg - 25 wt% Ca - 5 wt% Zn, HRTEM images taken from sites marked A, B and C. The relationship to MgO and α-Mg is observed.

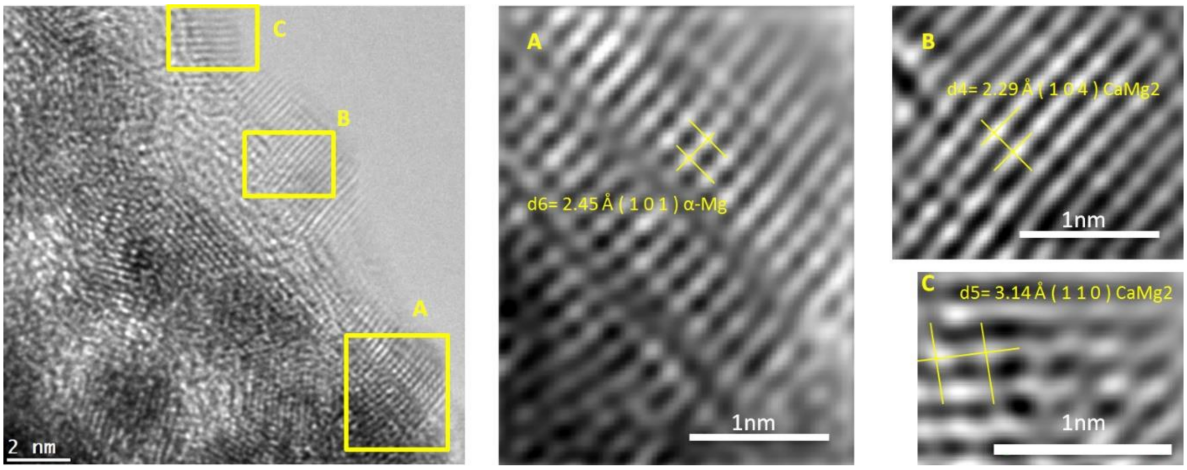

Figure 9. Plane identification with respect to interplanar space measurement on Mg - 25 wt% Ca - 5 wt% Zn, HRTEM images taken from sites marked A, B and C. The relationship between α-Mg and $CaMg_2$ is observed.

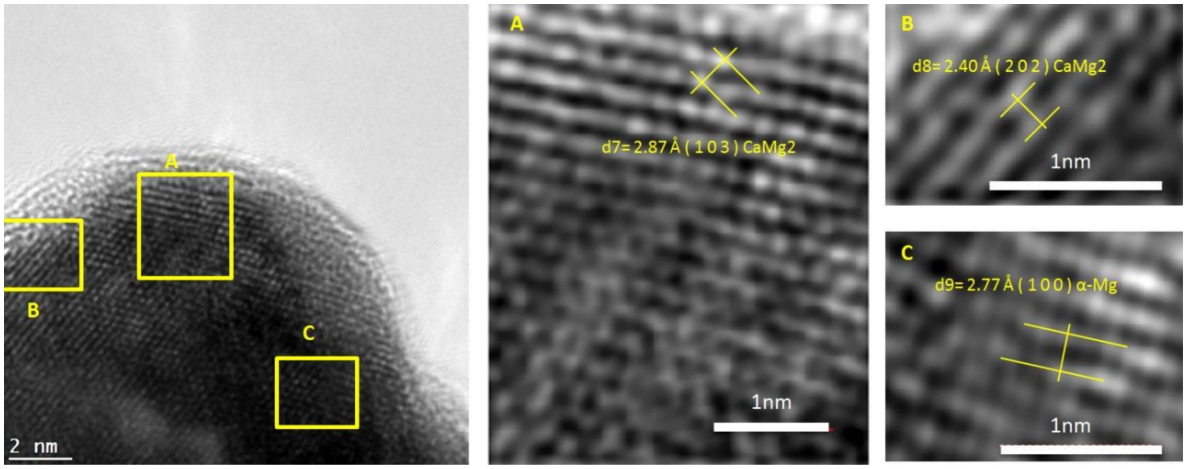

Figure 10. Plane identification with respect to interplanar space measurement on Mg - 25 wt% Ca - 5 wt% Zn, HRTEM images taken from sites marked A, B and C. The relationship between $CaMg_2$ and α-Mg is observed.

4.4. Micro-Indentation

The mechanical properties of the Mg - 25 wt% Ca - 5 wt% Zn alloy were determined in the longitudinal and transverse direction using micro-indentation. Nine individual measurements for each direction were made to map the areas of the material due to the brittleness presented.

Figure 11 shows the average values obtained from the nine longitudinal and transverse micro-indentation measurements. The standard deviation (SD) represents the average of the indentations made for each direction; they are not related to the exact place in the Mg - 25 wt% Ca - 5 wt% Zn material.

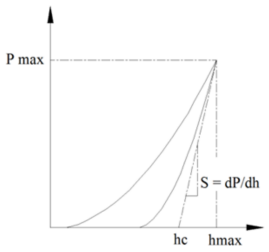

	Longitudinal (SD)	Transversal (SD)
Elastic Modulus, GPa	74.21 (2.3)	66.21 (2.5)
Hardness, HV	278.94 (0.061)	264.35 (0.082)
Pmax, mN	20.46	20.46
hmax, nm	531.18	481.75
S, mN/nm	0.2379	0.2137
hc, nm	418.62	410.96

Figure 11. Load-displacement curve, hmax: maximum penetration, S: tangent discharge curve (stiffness), hc: contact depth. Elastic moduli and hardness for Mg - 25 wt% Ca - 5 wt% Zn.

In Figures 12 and 13, the force-penetration depth and force-indentation curves of the average measurement corresponding to the transverse direction are observed. These values correspond to Pmax: 20.46 mN, hmax: 481.75 nm, S: 0.2137 mN/nm, hc: 410.96 nm.

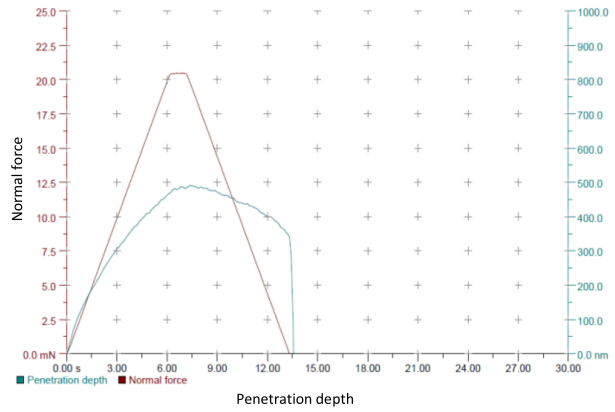

Figure 12. Force-Penetration depth.

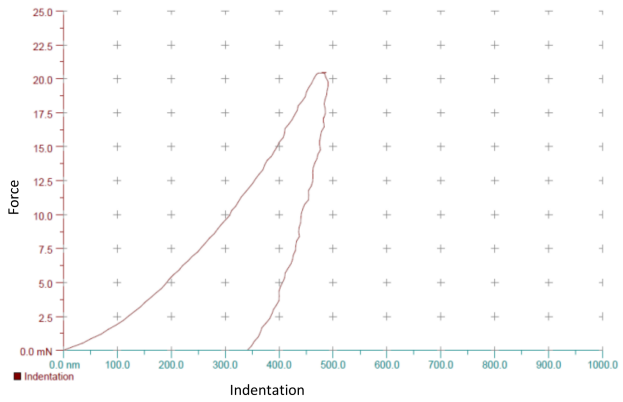

Figure 13. Force-Indentation.

4.5. Cell Viability

The Mg - 25 wt% Ca - 5 wt% Zn alloy extracts did not induce any change or impact on cell viability or morphology, ruling out any detrimental effects. (See Figure 14) The osmolality caused by Mg must be taken into account as an effect that will produce cellular stress [89].

It can be noted that in none of the serial solutions, including the concentration of 100% extract, was there a decrease in metabolic activity that affects cell viability. This result confirms that the selection of elements for a biomedical alloy from the foundry, as stated at the beginning of this work, is a key and avant-garde strategy for the development of new biomedical alloys. Work is still needed to improve the mechanical properties. However, this result will contribute to achieving the sanitary regulation of Mg as a biomaterial for the manufacture of implants. Ramírez et al. presented a definition of the natural process when selecting elements and called it bio-inspired design [6].

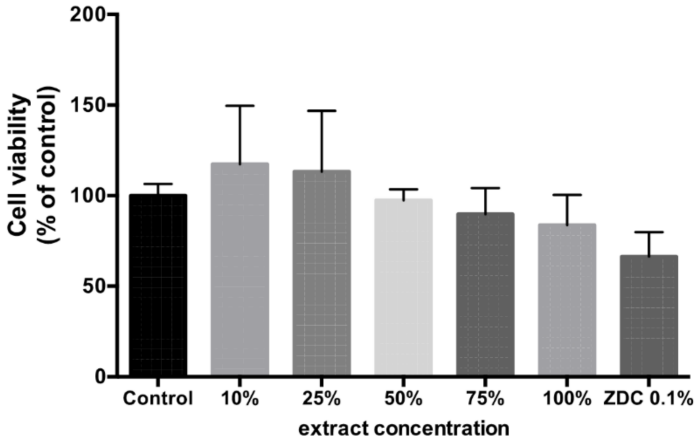

Figure 14. The effect of Mg - 25 wt% Ca - 5 wt% Zn extracts in the viability of L-929 murine fibroblasts. The graph represents results obtained after 48 h incubation with nonserial dilutions of Mg - 25 wt% Ca - 5 wt% Zn extracts as assayed by the neutral red uptake assay (n = 4). Data are expressed as media ± standard deviation in percentage relative to the control (cell culture medium). Note that there are not significant differences between treatments, $p > 0.05$.

The cell metabolic activity (viability) of adhered L-929 cells exposed to Mg - 25 wt% Ca - 5 wt% Zn original extracts was compared to untreated cells (negative control; CTRL) and cells treated with the cytotoxic zinc diethyldithiocarbamate (ZDC) after two days of same culture conditions (Figure 15A).

L-929 murine fibroblast experienced a not cytotoxic outcome in a dose-response fashion when exposed for 24 or 48 h to incremental concentrations of original extracts of Mg - 25 wt% Ca - 5 wt% Zn (Figure 15B). The effect induced by Mg - 25 wt% Ca - 5 wt% Zn extract on cell viability wasn't comparable to that of cytotoxic molecule Zinc diethyldithiocarbamate (ZDC 0.1%) Figure 14. There was no rounded or lised in the cells, monolayers and a growth are observed. On the other hand, in the cell cultures exposed to Mg - 25 wt% Ca - 5 wt% Zn extracts there is cell adhesion, but no evident intracytoplasmic granules and morphological changes; the % growth inhibition is observed. The Mg - 25 wt% Ca - 5 wt% Zn extracts did not induce any reduction in cell viability not in cell morphology, discarding any detrimental effect on cells.

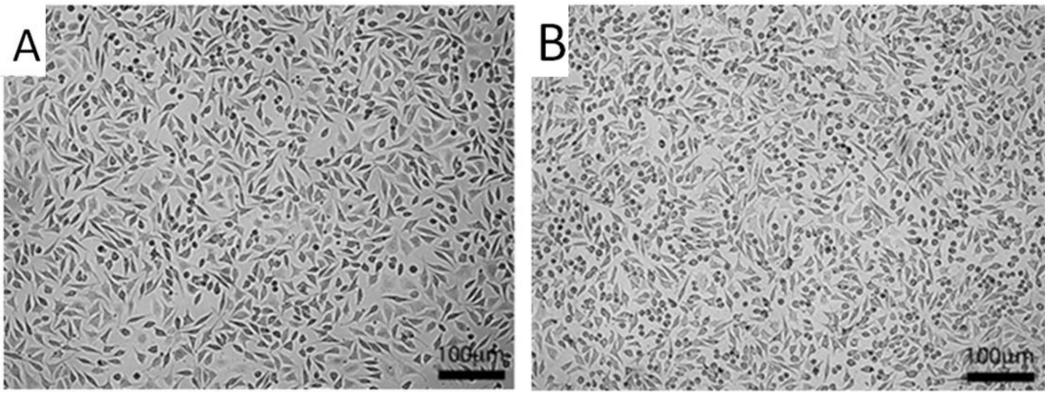

Figure 15. Representative micrographs of non-exposed cells (negative control; (**A**,**B**) cells exposed to the original extracts of Mg - 25 wt% Ca - 5 wt% Zn after two days of same culture conditions. Magnification 10×, scale bar 100 µm.

4.6. Validation by Finite Element Method, Load Progression versus Comparison to BDM

A FEM simulation was performed using Ansys 15 software to visualize the mechanical behavior of the alloy and its response to failure modes. From the information obtained from the experimental microindentation tests, a valid in silico model was built for comparison against DBM. The intention was to show its integrity and performance as an alternative to DBM material. An isotropic bi-linear simulation was performed creating the material Mg - 25 wt% Ca - 5 wt% Zn; the properties used were Young's modulus 74.2 GPa (Longitudinal), Poisson 0.30 (obtained by micro-indentation), using a uniaxial table to tabulate the behavior of the material. Tensile yield strength was configured at 50 MPa and tensile strength ultimate at 290 MPa; the deformation that the material can withstand corresponds to 0.017 mm/mm [72]. The model consists of 30,887 nodes and 17,779 SOLID 186 elements; large deflection was activated to control deformation (See Figure 16). The boundary conditions were one fixed support on the lateral face and the application of compressive force by 8.31 N. The maximum elastic deformation was 0.01703 mm/mm, while the maximum stress that it supported before failure corresponded to 0.447 MPa. When comparing these values with the mechanical properties of the DBM, it was verified that the proposed alloy Mg - 25 wt% Ca - 5 wt% Zn can be used as a viable alternative to replace cadaver bone. From the perspective of biocompatibility, the elements used and the products of the phases created do not represent a cytotoxic effect according to with ISO-10993. Mg, Ca and Zn have been related as elements that promote osseointegration and osteogenesis. Sudeep Paul, Anvari-Yazdi et al. demonstrated that elements such as Ca and Zn have a neutral effect on adipose-derived mesenchymal stem cells [101,102]. Chaoxing Zhang et al. demonstrated that Mg-Zn-Ca alloys possess antimicrobial properties and are promising options in bone repair [12,103]. Rahman et al. report that Mg base alloys can be enriched with antibiotics to improve their antibacterial performance [6,104–107].

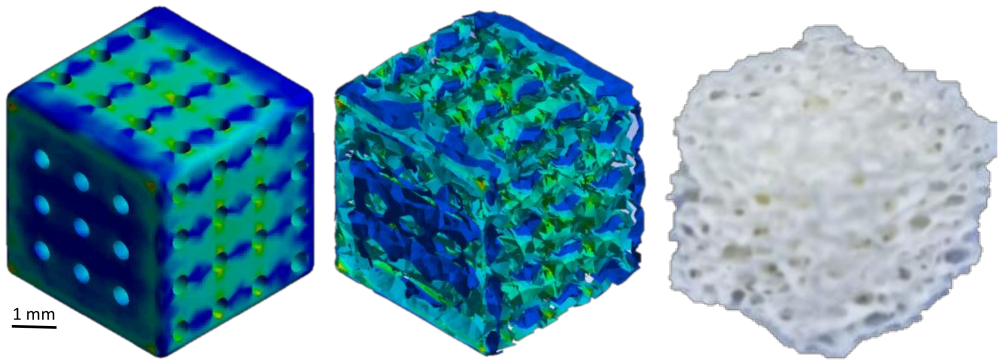

Figure 16. Scaffold load progression and comparison to DBM.

5. Discussion

Starting the process from a master alloy with the approximate percentages of the desired composition will be the best alternative due to economic-environmental viability for casting Mg alloys for biomedical purposes.

Regarding the release of harmful ions, Cicha et al. propose the use of ferritic elements for cardiovascular applications, in order to be able to recover dissolved metal ions with adherence of endothelial cells by magnetism and to evaluate the therapeutic benefit [108,109]. This would not be possible when using Mg base alloys, mainly due to the characteristic paramagnetic properties of Mg ions. If this study phenomenon is of interest, a good strategy would be to dope Mg with elements such as Nd to promote a partial recovery of metallic ions where the effect on Nd ions can be sampled. An advantage of its use is that Nd acts as a grain refiner, contributing to mechanical integrity; however, its toxicological potential has limited its use in medical devices [110,111]. One possible alternative is to use it at an exposure limit with biosecurity precautions that could be implemented through the magnetic cell recruitment technique proposed by Cicha.

The contribution of the $MgCa_2$ phase to the mechanical behavior of the alloy is related to the morphology of the eutectic lamellar phase providing the characteristic brittleness. This implies that the melting point of the phase is below the melting point of both main constituents. The solidification of interlocking sheets explains the nature of brittleness in the material. The development and medical use of Mg alloys have been limited due to the poor formation of sliding systems that induce low ductility, a process that becomes more complicated when elements are added to reinforce the matrix of the alloy [84]. The addition of pure elements such as Ca and Zn to form this base-Mg alloy will be restricted due to the solubility limits of the elements. Understanding the formation of each of the phases and checking the preferential orientation of the grain in the morphological characterization will indicate the affectation of Mg alloys when transformed by fusion or mechanical deformation, providing evidence that dynamic recrystallization occurs [112,113]. Park et al. have reported that both plastic deformation and the atomic diffusion process induce preferential orientation of the grain [59]. The existence of diffuse diffraction rings is an indicator of the replacement of Mg ions by Ca. This phenomenon, of cariation in intensity and circumference, was also reported by Bowen [86]. The crystalline orientation (texture) has an impact on the degradation of Mg alloys [58]. This impact is greater in the application, if the flow of the body fluid affects the normal orientation to the surface. When the surface of the Mg is exposed to the flow of a body fluid, the bio-erosion produced by the fluid influencing the material accelerates the degradation. To prolong the life of a Mg implant, it should be recommended in surgical techniques to take care of the placement, avoiding exposure of the implant to a blood flow that affects perpendicularly on the surface, since this effect can improve the performance of a medical device manufactured in Mg. Deepening the characterization of the texture of a MgCa implant depends largely on the behavior of the alloy; even when the texture is improved, the behavior of MgCa alloys will show tendencies towards brittleness [19,114]. Various efforts have been made to improve the casting process and consequently the mechanical properties of MgCa alloys [39]. However, no matter how much the process can be improved, it must be considered that the eutectic lamellar phases that originate will always be present in the incorporation of Ca to Mg. Homogenization due to improvements in the foundry offers to improve the biocompatibility [24,115–117]; however, the characteristics of the morphologies reported indicate a strong inclination towards fragility.

The mechanical properties are also affected by the orientation of the grain, causing microstructural changes due to the elongation of the grains themselves, which is reflected in their elastic components, inducing anisotropy [93,118–121].

The combination of SEM-EDS, XRD and TEM techniques allows us to understand the importance of each microstructural phase and its effect. Twins within the grains can prevent band dislocations and are related to material creep. The α-Mg phase normalizes the $MgCa_2$ matrix and prevents acceleration in degradation [122].

In Figure 4 a non-homogenized morphology can be seen, which is logical, since the ideal is to melt these materials under vacuum and centrifuge them. However, a diffusion of Zn over MgCa is achieved, which is the most important part of the work, because it allows us to carry out the evaluation of cell viability directly from the material.

Traces of pitting corrosion were observed during the SEM-EDS analysis, indicating that the alloy is resistant to corrosion, however, this corrosion will act as a stress concentrator and the degradation process will start as soon as the material is superficially affected, affecting the mechanical properties and leading to eventual dissolution [123]. The distribution of mechanical stresses is not homogeneous throughout the material, due to the crystallographic orientation, and to the second phases that initiate the nucleation of the material, also generating cracks, pores and precipitates. Cesarz et al. reported that dissolved Ca particles can precipitate and form anticorrosive layers that slow down degradation [124,125].

It is possible that Zn was not detected because there were only small amounts in the alloy; however, it has already been reported that in Mg-Zn diffraction, only the α-Mg phase diffracts intensity. Yan Jingli reported that by decreasing the scanning speed during XRD analysis, the formation of weak diffraction peaks of the $MgZn_2$ phase is revealed, such as those formed and not identified in the result shown for XRD (See Figure 5). The lack of identification of Zn phases can be attributed to multiple causes, including a possible preferential reorientation during the preparation of the specimens. Unfortunately Yan Jingli does not report a scanning speed for the detection of the $MgZn_2$ phases by XRD. The value used in this work corresponds to scan step time [s], 59.69, which suggests that a lower speed should be used. An atomic rearrangement by a mechanism such as hardening deformation will increase the intensity of Zn [114]. The structured lattice arrangement in the generation of quasi-crystalline phases has shown excellent mechanical properties, reducing the coefficient of friction and resistance to corrosion [126].

This alloy shows a phenomenon due to precipitates in which the Zn peaks do not appear. This could be partly due to the fact that a rearrangement is required and what exists is a preferential orientation due to the sanding process. When polishing the sample or when the elements were melted, they are superficially deposited and agglomerated, which causes them to be removed with sandpaper when polishing or a preferential reorientation occurs.

Increasing the temperature above 200 °C on the surface of an implant made of MgZn alloy should be avoided in order to minimize microstructural modification [47,127]. Galvanic corrosion that occurs between Mg and Zn generates a rapid dissolution of secondary phases, weakening the Mg matrix; this explains the potential for bioactivity generated by these elements acting together in an alloy.

Tripathy reported that solid Zn-Ca solutions could be prepared in the entire range of compositions, although incoherent values of the grating parameters and diffraction patterns were observed. Through the study by the Rietveld method, it was determined that the parameters change when adding Zn when a modification exists [98,100].

The results shown correspond to the average value of nine tests for longitudinal and transverse orientation. In the upper half of the load vs. displacement curve are the data with which the elastic modulus (E) and hardness H (VK) are calculated). During load application, elastic and plastic deformations occur under the indenter as the contacts change deeper. The discharge part of the curve is dominated by elastic displacements. The diamond indenter has a V = 0.07 and an E = 1140 GPa, the Mg - 25 wt% Ca - 5 wt% Zn material has a V = 0.30; through sensitivity studies it has been determined that variations in the range of 0.2–0.4 in V will present a variation the elastic modulus E not greater than 8%.

The determination of the elastic modulus derived from the Oliver and Pharr method consists of an average of the isotropic elastic constants; however, for an anisotropic material it has been determined that the measurements are inclined towards the elastic modulus in the direction of the test. For a material that exhibits an HCP structure, the determination of the elastic modulus only considers the normal direction, underestimating the other elastic

components by mono-crystallinity. The influence of the elastic constants that occur in an orthotropic material are of vital importance for understanding the behavior of the material.

Fibroblasts tend to adhere to the surface and show an elongated polygonal morphology, if they are healthy and normal. If, on the other hand they present a degraded appearance and spherical morphology in addition to the detachment of the surface, they usually indicate cell death, which was not observed.

As complementary perspectives to cell viability, it is widely recommended to use analyses that represent cell dynamics by monitoring cell properties in real time, it is desired know the adherence to non-folding surfaces, proliferation, and cell migration [104,128–131].

Viz, Yang et al. reported an increase in cell viability of osteoblasts reducing DNA damage in the formation of new bone using Zn-Mg alloys [132].

6. Conclusions

As a general conclusion:

(1) The optimization of the casting process of a Mg-Ca-Zn alloy has a microstructural limit, which is due to the eutectic mixture. Even when the process is optimized, a fine dispersion between phases will continue to appear, resulting in an origin for crack nucleation.

(2) The period of exposure to elements such as Mg, Ca and Zn within the body causes pathophysiology to occur. Being clear about the period of exposure in days for the effects to occur is a key factor in understanding the beneficial effect that they can contribute prior to hydrolytic degradation in vivo.

(3) Zn improves the mechanical response when hardening this type of alloys, however, exceeding the permitted limits damages the toxicological limit, which will have an impact on cell viability. Viz, Zhuang, et al. reported Zn dose-dependent and over-boosted concentration caused cell death due to cytotoxicity [90]. Elements such as Sr and Ca have been reported to be able to counteract and reduce the toxicity of Zn [133,134]. Lu et al. reported that Zn promotes the absorption of the hydrogen that is released due to the Mg reaction in vitro [135].

(4) An annealing process on this alloy will dissolve the intermetallic phases that occur and help to homogenize the distribution of the solutes in the Mg matrix, however, the precipitates could have a detrimental effect on the corrosion rate.

(5) The melting of Mg, Ca and Zn and their modification by diffusion are possible from MgCa master alloys. This process manages to diffuse Zn in powder over MgCa; the use of a vacuum system will allow a clean atmosphere. Thus, the alloy microstructure and grain size will be finer.

(6) The coatings on Mg alloys are very important, depending on the type of medical application for which they are to be used. A coating used on Mg alloys has the purpose of increasing the implant time in vivo, which will provide mechanical resistance to the fracture; for this application, using a coating that reduces the appearance of pitting corrosion is a multidisciplinary strategy that will completely depend on the initial weeks, during which it is necessary to maintain the mechanical integrity of the implant. It is suggested to evaluate a coating based on Chitosan that allows the maintenance of an intact implant surface for six weeks to limit the places where crack propagation can begin.

(7) The elastic modulus was 74.2 GPa for the longitudinal direction and 66.2 GPa in the transverse direction. This was determined from the repetitions of the test, which showed that the elastic modulus was always higher in the longitudinal direction, while the hardness followed a similar pattern, reported as 278.9 and 264.3 HV in longitudinal and transverse direction, respectively. An anisotropy condition between the longitudinal and transverse direction is fulfilled by having different elastic modulus and hardness. The determination of the elastic modulus and hardness in each triad for each degree of freedom could be useful to relate to the orientation of the planes and to have the behavior of the elastic constants characterized.

(8) The ideal application for this type of alloy corresponds to anatomical sites where it is only exposed to gravity and forces caused by muscles, such as the movement of the upper extremities and the skull.
(9) Experimenting with texture control techniques on Mg alloys could be an effective strategy to determine the ideal method for manufacturing Mg-based implants. However, the mechanical behavior of Mg depends on the adequate relationship between the volumetric fraction of elements and the formation of lamellar long period stacking order (LPSO) secondary phases [127,136,137].

The method shown for the diffusion of Zn in MgCa solves technical problems related to equipment and facilities with high costs, allowing for the evaluation of the structural effect in an approximation work, which shows the microstructural viability of this alloy and its limitations. The frontiers of the existing methods for the incorporation of elements with low solubility for Mg alloys have been clarified, evaluating in three smelting experiments, and reporting a heating curve, stabilization period, and cooling curve. Induction casting results have partially diffused Zn into the MgCa microstructure.

Zn traces were quantitatively identified in the diffused MgCa sample, even though this phenomenon requires exhaustive investigation. The cell viability of MgCa was not affected by Zn, and no morphological changes occured in cells.

7. Declarations

It is declared by the authors of this work that there is no conflict of interest regarding the following.

- Ethics approval and consent to participate: N/A
- Consent for publication: N/A
- Availability of data and materials: OK
- Competing interests: No conflict of interest.
- Funding
- N/A
- Authors' contributions

Author Contributions: L.H.C.B. contributed to the writing of the document, elaboration of the selection process of elements and conduction of the casting process, sample preparation and facilities for the rest of the essays presented in the manuscript. This included support in the casting process from the preparation of molds in each of the castings carried out to the weighing and loading of the elements. A.T.C., performed the analysis of the samples by SEM-EDS, TEM, by supporting the documentation of this manuscript, provided equipment to perform the experimentation by micro-indentation. (L.H.C.B. & A.T.C.) that they can share any information requested during the peer review process in the same way during the manuscript acceptance process. All authors have read and agreed to the published version of the manuscript.

Funding: This research received no external funding.

Institutional Review Board Statement: Not applicable.

Informed Consent Statement: Not applicable.

Data Availability Statement: Not applicable.

Acknowledgments: Thanks to Hugo Esquivel Solis and CIATEJ, for the unconditional support to perform biological tests on specimens and for their objective view of the work. Thanks to CIQA and Enrique Díaz Barriga for their support in preparing the FIB samples for crystallographic analysis. Thanks to Arturo Juarez for the advice provided during the casting process. Special thanks to Marco Antonio Loudovic Hernandez Rodriguez and Jonathan Puente de Leon for their support in the preparation of equipment and containers. A special thanks to Eduardo Nuñez Perez for his unconditional support, thanks to his feedback and his comments this work has been enriched. Thanks to Professor Raúl Lesso Arroyo† for his advice and guidance.

Conflicts of Interest: The authors declare that there is no conflict of interest regarding the publication of this paper.

Abbreviations

magnesium (Mg), calcium (Ca), zinc (Zn), demineralized bone matrix (DBM), American Association of Tissue Banks (AATB), bone morphogenetic protein (BMP), craniomaxillofacial (CMF), long period stacking order (LPSO).

References

1. Holtzclaw, D.; Toscano, N.; Eisenlohr, L.; Callan, D. The safety of bone allografts used in dentistry: A review. *J. Am. Dent. Assoc.* **2008**, *139*, 1192–1199. [CrossRef]
2. Salyer, K.E.; Taylor, D.P. Bone grafts in craniofacial surgery. *Clin. Plast. Surg.* **1987**, *14*, 27–35. [CrossRef]
3. Wang, J.C.; Alanay, A.; Mark, D. A comparison of commercially available demineralized bone matrix for spinal fusion. *Eur. Spine J.* **2007**, *16*, 1233–1240. [CrossRef] [PubMed]
4. Maier, H.J.; Julmi, S. Magnesium Alloys for Open-Pored Bioresorbable Implants. *JOM* **2020**, *72*, 1859–1869. [CrossRef]
5. Liu, C.; Ren, Z.; Xu, Y.; Pang, S.; Zhao, X.; Zhao, Y. Biodegradable Magnesium Alloys Developed as Bone Repair Materials: A Review. *Scanning* **2018**, *2018*, 19. [CrossRef]
6. Ramirez Patino, J.F. Bioresorbable Magnesium-Based Sponge and Foam Materials. Methods and Devices. Worldwide Applications WO 2018/187756 A1, 11 October 2018.
7. Becerra, L.H.C.; Rodríguez, M.A.L.H.; Solís, H.E.; Arroyo, R.L.; Castro, A.T. Bio-inspired biomaterial Mg-Zn-Ca: A review of the main mechanical and biological properties of Mg-based alloys. *Biomed. Phys. Eng. Express* **2020**, *6*, 042001. [CrossRef]
8. Li, X.; Niu, Y.; Guo, H.; Chen, H.; Li, F.; Zhang, J.; Chen, W.; Wu, Z.; Deng, Y.; Wei, J.; et al. Preparation and osteogenic properties of magnesium calcium phosphate biocement scaffolds for bone regeneration. *J. Instrum.* **2013**, *8*, C07010. [CrossRef]
9. Deng, J.; Ye, J.; Zhao, Y.; Zhu, Y.; Wu, T.; Zhang, C.; Dong, L.; Ouyang, H.; Cheng, X.; Wang, X. ZnO and Hydroxyapatite-Modified Magnesium Implant with a Broad Spectrum of Antibacterial Properties and a Unique Minimally Invasive Defined Degrading Capability. *ACS Biomater. Sci. Eng.* **2019**, *5*, 4285–4292. [CrossRef]
10. Alshaaer, M.; Abdel-Fattah, E.; Saadeddin, I.; al Battah, F.; Issa, K.; Saffarini, G. The effect of natural fibres template on the chemical and structural properties of Biphasic Calcium Phosphate scaffold. *Mater. Res. Express* **2020**, *7*, 065405. [CrossRef]
11. Moradi, E.; Ebrahimian-Hosseinabadi, M.; Khodaei, M.; Toghyani, S. Magnesium/Nano-Hydroxyapatite porous biodegradable composite for biomedical applications. *Mater. Res. Express* **2019**, *6*, 075408. [CrossRef]
12. Ong, K.L.; Yun, B.M.; White, J.B. New biomaterials for orthopedic implants. *Orthop. Res. Rev.* **2015**, *7*, 107–130. [CrossRef]
13. U.S. Food & Drug Administration. Jurisdictional Update: Human Demineralized Bone Matrix. 2018. Available online: https://www.fda.gov/combination-products/jurisdictional-updates/jurisdictional-update-human-demineralized-bone-matrix (accessed on 12 October 2021).
14. Wang, J.L.; Xu, J.K.; Hopkins, C.; Chow, D.H.K.; Qin, L. Biodegradable Magnesium-Based Implants in Orthopedics—A General Review and Perspectives. *Adv. Sci.* **2020**, *7*, 1902443. [CrossRef] [PubMed]
15. Gao, C.; Peng, S.; Feng, P.; Shuai, C. Bone biomaterials and interactions with stem cells. *Bone Res.* **2017**, *5*, 17059. [CrossRef] [PubMed]
16. Amerstorfer, F.; Fischerauer, S.F.; Fischer, L.; Eichler, J.; Draxler, J.; Zitek, A.; Meischel, M.; Martinelli, E.; Kraus, T.; Hann, S.; et al. Long-term in vivo degradation behavior and near-implant distribution of resorbed elements for magnesium alloys WZ21 and ZX50. *Acta Biomater.* **2016**, *42*, 440–450. [CrossRef] [PubMed]
17. Lesz, S.; Kraczla, J.; Nowosielski, R. Structure and compression strength characteristics of the sintered Mg–Zn–Ca–Gd alloy for medical applications. *Arch. Civ. Mech. Eng.* **2018**, *18*, 1288–1299. [CrossRef]
18. Bakhsheshi-Rad, H.R.; Abdellahi, M.; Hamzah, E.; Ismail, A.F.; Bahmanpour, M. Modelling corrosion rate of biodegradable magnesium-based alloys: The case study of Mg-Zn-RE-xCa (x = 0, 0.5, 1.5, 3 and 6 wt%) alloys. *J. Alloys Compd.* **2016**, *687*, 630–642. [CrossRef]
19. Wang, Y.; Liu, G.; Wei, Y.; Qiao, Y. Effects of magnesium-calcium alloys with different calcium content on their mechanical properties. *IOP Conf. Ser. Mater. Sci. Eng.* **2020**, *735*, 012010. [CrossRef]
20. Sezer, N.; Evis, Z.; Kayhan, S.M.; Tahmasebifar, A.; Koç, M. Review of magnesium-based biomaterials and their applications. *J. Magnes. Alloy.* **2018**, *6*, 23–43. [CrossRef]
21. Pulido-gonzález, N.; Torres, B.; Rodrigo, P.; Hort, N.; Rams, J. Microstructural, mechanical and corrosion characterization of an as-cast Mg–3Zn–0.4Ca alloy for biomedical applications. *J. Magnes. Alloy.* **2020**, *8*, 510–522. [CrossRef]
22. Radha, R.; Sreekanth, D. Insight of magnesium alloys and composites for orthopedic implant applications—A review. *J. Magnes. Alloy.* **2017**, *5*, 286–312. [CrossRef]
23. Xu, T.O.; Kim, H.S.; Stahl, T.; Nukavarapu, S.P. Self-neutralizing PLGA/magnesium composites as novel biomaterials for tissue engineering. *Biomed. Mater.* **2018**, *13*, 035013. [CrossRef] [PubMed]
24. Gu, X.N.; Li, N.; Zhou, W.R.; Zheng, Y.F.; Zhao, X.; Cai, Q.Z.; Ruan, L. Corrosion resistance and surface biocompatibility of a microarc oxidation coating on a Mg-Ca alloy. *Acta Biomater.* **2011**, *7*, 1880–1889. [CrossRef] [PubMed]
25. Sedelnikova, M.B.; Komarova, E.G.; Sharkeev, Y.P.; Tolkacheva, T.V.; Sheikin, V.V.; Egorkin, V.S.; Mashtalyar, D.V.; Kazakbaeva, A.A.; Schmidt, J. Characterization of the Micro-Arc coatings containing β-tricalcium phosphate particles on Mg-0.8Ca alloy. *Metals* **2018**, *8*, 238. [CrossRef]

26. Farahany, S.; Bakhsheshi-Rad, H.R.; Idris, M.H.; Kadir, M.R.A.; Lotfabadi, A.F.; Ourdjini, A. In-situ thermal analysis and macroscopical characterization of Mg-xCa and Mg-0.5Ca-xZn alloy systems. *Thermochim. Acta* **2012**, *527*, 180–189. [CrossRef]
27. Zeng, R.; Lan, Z.; Kong, L.; Huang, Y.; Cui, H. Characterization of calcium-modified zinc phosphate conversion coatings and their influences on corrosion resistance of AZ31 alloy. *Surf. Coat. Technol.* **2011**, *205*, 3347–3355. [CrossRef]
28. Yu, S.Z.Q.; Wang, C.; Yang, J.; Guo, C. Mineralized collagen/Mg-Ca alloy combined scaffolds with improved biocompatibility for enhanced bone response following tooth extraction. *Biomed. Mater.* **2018**, *13*, 065008. [CrossRef]
29. Feyerabend, R.W.F.; Witte, F.; Vogt, C.; Fischer, J.; Schreyer, A.; Kainer, K.U.; Hort, N. In Vitro Testing of Magnesium Alloys—Challenges and Options. In Proceedings of the 8th International Conference on Magnesium Alloys and their Applications, Weimar, Germany, 26–29 October 2021.
30. Sharma, P.; Chattopadhyaya, S.; Singh, N.K. A review on magnetically supported gas metal arc welding process for magnesium alloys. *Mater. Res. Express* **2019**, *6*, 082002. [CrossRef]
31. Toghyani, S.; Khodaei, M. Fabrication and characterization of magnesium scaffold using different processing parameters. *Mater. Res. Express* **2018**, *5*, 035407. [CrossRef]
32. Guan, R.g.; Cipriano, A.F.; Zhao, Z.; Lock, J.; Tie, D.; Zhao, T.; Cui, T.; Liu, H. Development and evaluation of a magnesium-zinc-strontium alloy for biomedical applications—Alloy processing, microstructure, mechanical properties, and biodegradation. *Mater. Sci. Eng. C* **2013**, *33*, 3661–3669. [CrossRef]
33. Annur, D.; Franciska, P.; Erryani, A.; Amal, M.I.; Sitorus, L.S.; Kartika, I. The synthesis and characterization of Mg-Zn-Ca alloy by powder metallurgy process. *AIP Conf. Proc.* **2016**, *1725*, 19. [CrossRef]
34. Jin, C.; Narayan, R.J. Structural and optical properties of hexagonal Mg xZn 1-xO thin films. *J. Electron. Mater.* **2006**, *35*, 869–876. [CrossRef]
35. Mironov, V.; Trusk, T.; Kasyanov, V.; Little, S.; Swaja, R.; Markwald, R. Biofabrication: A 21st century manufacturing paradigm. *Biofabrication* **2009**, *1*, 022001. [CrossRef] [PubMed]
36. Ni, M.; Niu, W.; Wong, D.W.C.; Zeng, W.; Mei, J.; Zhang, M. Finite element analysis of locking plate and two types of intramedullary nails for treating mid-shaft clavicle fractures. *Injury* **2016**, *47*, 1618–1623. [CrossRef] [PubMed]
37. Senkov, O.N.; Scott, J.M. Glass forming ability and thermal stability of ternary Ca-Mg-Zn bulk metallic glasses. *J. Non. Cryst. Solids* **2005**, *351*, 3087–3094. [CrossRef]
38. Gu, X.; Zheng, Y.; Zhong, S.; Xi, T.; Wang, J.; Wang, W. Corrosion of, and cellular responses to Mg-Zn-Ca bulk metallic glasses. *Biomaterials* **2010**, *31*, 1093–1103. [CrossRef] [PubMed]
39. Geanta, V.; Voiculescu, I.; Kelemen, H.; Manu, D.; Molnár, G.; Kelemen, G. Mg-Ca-Zn bio-degradable light alloys produced in a levitation induction melting furnace. *Int. J. Appl. Electromagn. Mech.* **2020**, *63*, S69–S78. [CrossRef]
40. Hrapkowicz, B.; Lesz, S.T. Characterization of Ca 50 Mg 20 Zn 12 Cu 18 Alloy. *Arch. Foundry Eng.* **2019**, *19*, 75–82. [CrossRef]
41. Ma, S.; Xing, F.; Ta, N.; Zhang, L. Kinetic modeling of high-temperature oxidation of pure Mg. *J. Magnes. Alloy.* **2020**, *8*, 819–831. [CrossRef]
42. Shahri, Z.; Allahkaram, S.R.; Soltani, R.; Jafari, H. Optimization of plasma electrolyte oxidation process parameters for corrosion resistance of Mg alloy. *J. Magnes. Alloy.* **2020**, *8*, 431–440. [CrossRef]
43. Kumar, A.; Pandey, P.M. Development of Mg based biomaterial with improved mechanical and degradation properties using powder metallurgy. *J. Magnes. Alloy.* **2020**, *8*, 883–898. [CrossRef]
44. Yang, M.; Liu, D.; Zhang, R.; Chen, M. Microstructure and Properties of Mg-3Zn-0.2Ca Alloy for Biomedical Application. *Xiyou Jinshu Cailiao Yu Gongcheng/Rare Met. Mater. Eng.* **2018**, *47*, 93–98. [CrossRef]
45. Smith, C.E. Aggie Digital Collections and Scholarship Processing and Characterization Of Innovative Magnesium Alloys for Biodegradable Orthopaedic Implants. Ph.D. Thesis, 2014. Available online: https://digital.library.ncat.edu/dissertations/102 (accessed on 12 October 2021).
46. Bell, S.; Ajami, E.; Davies, J.E. An improved mechanical testing method to assess bone-implant anchorage. *J. Vis. Exp.* **2014**, *9*, 1–10. [CrossRef] [PubMed]
47. Fischerauer, S.F. Preclinical Characterization of Bioresorbable Magnesium Implants for Osteosynthesis. Ph.D. Thesis, Medical University of Graz, Graz, Austria, 2015.
48. Liu, C.; Wang, J.; Gao, C.; Wang, Z.; Zhou, X.; Tang, M.; Yu, K.; Deng, Y. Enhanced osteoinductivity and corrosion resistance of dopamine/gelatin/rhBMP-2–coated β-TCP/Mg-Zn orthopedic implants: An in vitro and in vivo study. *PLoS ONE* **2020**, *15*, e0228247. [CrossRef] [PubMed]
49. Hiromoto, S.; Itoh, S.; Noda, N.; Yamazaki, T.; Katayama, H.; Akashi, T. Osteoclast and osteoblast responsive carbonate apatite coatings for biodegradable magnesium alloys. *Sci. Technol. Adv. Mater.* **2020**, *21*, 346–358. [CrossRef]
50. Chang, Y.H.; Tseng, C.C.; Chao, C.Y.; Chen, C.H.; Lin, S.Y.; Du, J.K. Mg-Zn-Ca alloys for hemostasis clips for vessel ligation: In vitro and in vivo studies of their degradation and response. *Materials* **2020**, *13*, 3039. [CrossRef]
51. Sarkar, K.; Kumar, V.; Devi, K.B.; Ghosh, D.; Nandi, S.K.; Roy, M. Anomalous in Vitro and in Vivo Degradation of Magnesium Phosphate Bioceramics: Role of Zinc Addition. *ACS Biomater. Sci. Eng.* **2019**, *5*, 5097–5106. [CrossRef]
52. Ostrowski, N.; Lee, B.; Hong, D.; Enick, P.N.; Roy, A.; Kumta, P.N. Synthesis, Osteoblast, and Osteoclast Viability of Amorphous and Crystalline Tri-Magnesium Phosphate. *ACS Biomater. Sci. Eng.* **2015**, *1*, 52–63. [CrossRef]
53. Ibrahim, H.; Esfahani, S.N.; Poorganji, B.; Dean, D.; Elahinia, M. Resorbable bone fixation alloys, forming, and post-fabrication treatments. *Mater. Sci. Eng. C* **2017**, *70*, 870–888. [CrossRef]

54. Gao, J.H.; Guan, S.K.; Chen, J.; Wang, L.G.; Zhu, S.J.; Hu, J.H.; Ren, Z.W. Fabrication and characterization of rod-like nano-hydroxyapatite on MAO coating supported on Mg-Zn-Ca alloy. *Appl. Surf. Sci.* **2011**, *257*, 2231–2237. [CrossRef]
55. Xin, Y.; Hu, T.; Chu, P.K. Influence of Test Solutions on In Vitro Studies of Biomedical Magnesium Alloys. *J. Electrochem. Soc.* **2010**, *157*, C238–C243. [CrossRef]
56. Yan, Y.; Chu, X.; Luo, X.; Xu, X.; Zhang, Y.; Dai, Y.; Li, D.; Chen, L.; Xiao, T.; Yu, K. A homogenous microstructural Mg-based matrix model for orthopedic application with generating uniform and smooth corrosion product layer in Ringer's solution: Study on biodegradable behavior of Mg-Zn alloys prepared by powder metallurgy as a case. *J. Magnes. Alloy.* **2021**, *9*, 225–240. [CrossRef]
57. Vinogradov, A.; Vasilev, E.; Kopylov, V.I.; Linderov, M.; Brilevesky, A.; Merson, D. High performance fine-grained biodegradable Mg-Zn-Ca alloys processed by severe plastic deformation. *Metals* **2019**, *9*, 186. [CrossRef]
58. Priyanto, T.H.; Insani, A.; Muslih, R.; Bharoto. Texture Analysis on the AZ31 Magnesium Alloy Using Neutron Diffraction Method. *J. Phys. Conf. Ser.* **2020**, *1436*, 235. [CrossRef]
59. Park, M.; Kim, K. Basal texture formation behavior of M1 magnesium alloy during high-temperature compression deformation. *J. Phys. Conf. Ser.* **2019**, *1270*. [CrossRef]
60. Xie, J.; Zhang, J.; You, Z.; Liu, S.; Guan, K.; Wu, R.; Wang, J.; Feng, J. Towards developing Mg alloys with simultaneously improved strength and corrosion resistance via RE alloying. *J. Magnes. Alloy.* **2021**, *9*, 41–56. [CrossRef]
61. Du, P.; Furusawa, S.; Furushima, T. Microstructure and performance of biodegradable magnesium alloy tubes fabricated by local-heating-assisted dieless drawing. *J. Magnes. Alloy.* **2020**, *8*, 614–623. [CrossRef]
62. Shi, Z.Z.; Chen, H.T.; Zhang, K.; Dai, F.Z.; Liu, X.F. Crystallography of precipitates in Mg alloys. *J. Magnes. Alloy.* **2021**, *9*, 416–431. [CrossRef]
63. Afandi, R.; Sutiyoko; Lutiyatm. Characteristic modifications of magnesium and its alloy for future implant material—Review. *J. Phys. Conf. Ser.* **2020**, *1517*. [CrossRef]
64. Janeček, M.; Krajňák, T.; Minárik, P.; Čížek, J.; Stráská, J.; Stráský, J. Structural stability of ultra-fine grained magnesium alloys processed by equal channel angular pressing. *IOP Conf. Ser. Mater. Sci. Eng.* **2017**, *194*, 12022. [CrossRef]
65. Zheng, M.; Xu, G.; Liu, D.; Zhao, Y.; Ning, B.; Chen, M. Study on the Microstructure, Mechanical Properties and Corrosion Behavior of Mg-Zn-Ca Alloy Wire for Biomaterial Application. *J. Mater. Eng. Perform.* **2018**, *27*, 1837–1846. [CrossRef]
66. Kim, Y.-H.; Yoo, H.-S.; Son, H.-T. Microstructure and Mechanical Properties of Mg–11Li–6Zn–0.6Zr–0.4Ag–0.2Ca–x Y Alloys. *J. Nanosci. Nanotechnol.* **2018**, *18*, 6304–6308. [CrossRef]
67. Song, G. Control of biodegradation of biocompatable magnesium alloys. *Corros. Sci.* **2007**, *49*, 1696–1701. [CrossRef]
68. Hamidi, M.F.F.A.; Harun, W.S.W.; Samykano, M.; Ghani, S.A.C.; Ghazalli, Z.; Ahmad, F.; Sulong, A.B. A review of biocompatible metal injection moulding process parameters for biomedical applications. *Mater. Sci. Eng. C* **2018**, *78*, 1263–1276. [CrossRef]
69. Vlček, M.; Lukáč, F.; Kudrnová, H.; Smola, B.; Stulíková, I.; Luczak, M.; Szakács, G.; Hort, N.; Willumeit-Römer, R. Microhardness and in vitro corrosion of heat-treated Mg-Y-Ag biodegradable alloy. *Materials* **2017**, *10*, 55. [CrossRef]
70. Li, Z.; Gu, X.; Lou, S.; Zheng, Y. The development of binary Mg-Ca alloys for use as biodegradable materials within bone. *Biomaterials* **2008**, *29*, 1329–1344. [CrossRef] [PubMed]
71. Cha, P.R.; Han, H.S.; Yang, G.F.; Kim, Y.C.; Hong, K.H.; Lee, S.C.; Jung, J.Y.; Ahn, J.P.; Kim, Y.Y.; Cho, S.Y.; et al. Biodegradability engineering of biodegradable Mg alloys: Tailoring the electrochemical properties and microstructure of constituent phases. *Sci. Rep.* **2013**, *3*, 2367. [CrossRef] [PubMed]
72. Li, Y.C.; Li, M.H.; Hu, W.Y.; Hodgson, P.D.; Wen, C.E. Biodegradable Mg-Ca and Mg-Ca-Y Alloys for Regenerative Medicine. *Mater. Sci. Forum* **2010**, *654–656*, 2192–2195. [CrossRef]
73. Li, T.; He, Y.; Zhang, H.; Wang, X. Microstructure, mechanical property and in vitro biocorrosion behavior of single-phase biodegradable Mg-1.5Zn-0.6Zr alloy. *J. Magnes. Alloy* **2014**, *2*, 181–189. [CrossRef]
74. Prakasam, M.; Locs, J.; Salma-Ancane, K.; Loca, D.; Largeteau, A.; Berzina-Cimdina, L. Biodegradable Materials and Metallic Implants—A Review. *J. Funct. Biomater.* **2017**, *8*, 44. [CrossRef]
75. Lu, Y.; Bradshaw, A.R.; Chiu, Y.L.; Jones, I.P. Effects of secondary phase and grain size on the corrosion of biodegradable Mg-Zn-Ca alloys. *Mater. Sci. Eng. C* **2015**, *48*, 480–486. [CrossRef]
76. Sikora-Jasinska, M.; Mostaed, E.; Mostaed, A.; Beanland, R.; Mantovani, D.; Vedani, M. Fabrication, mechanical properties and in vitro degradation behavior of newly developed Zn Ag alloys for degradable implant applications. *Mater. Sci. Eng. C* **2017**, *77*, 1170–1181. [CrossRef]
77. Jia, H.M.; Feng, X.H.; Yang, Y.S. Microstructure of directionally solidified Mg-Zn alloy with different growth rates. *Mater. Sci. Forum* **2015**, *816*, 411–417. [CrossRef]
78. Bakhsheshi-Rad, H.R.; Hamzah, E.; Fereidouni-Lotfabadi, A.; Daroonparvar, M.; Yajid, M.A.M.; Mezbahul-Islam, M.; Kasiri-Asgarani, M.; Medraj, M. Microstructure and bio-corrosion behavior of Mg-Zn and Mg-Zn-Ca alloys for biomedical applications. *Mater. Corros.* **2014**, *65*, 1178–1187. [CrossRef]
79. Zivić, F.; Grujović, N.; Manivasagam, G.; Richard, C.; Landoulsi, J.; Petrović, V. The potential of magnesium alloys as bioabsorbable/biodegradable implants for biomedical applications. *Tribol. Ind.* **2014**, *36*, 67–73.
80. Tao, J.X.; Zhao, M.-C.; Zhao, Y.-C.; Yin, D.-F.; Liu, L.; Gao, C.; Shuai, C.; Atrens, A. Influence of graphene oxide (GO) on microstructure and biodegradation of ZK30-xGO composites prepared by selective laser melting. *J. Magnes. Alloy.* **2020**, *8*, 952–962. [CrossRef]

81. Medina, S.; Mendoza, E.; Meza, J.M. Comportamiento microestructural de una fundición de magnesio puro con control en la temperatura de solidificación. *Univ. Tecnológica Pereira, Scientia Tech. Año XXII* **2017**, *22*, 145–149. [CrossRef]
82. Wang, K.; Dou, X.; Wang, J.; Huang, Y.; Gavras, S.; Hort, N.; Liu, S.; Hu, H.; Wang, J.; Pan, F. Achieving enhanced mechanical properties in Mg-Gd-Y-Zn-Mn alloy by altering dynamic recrystallization behavior via pre-ageing treatment. *Mater. Sci. Eng. A* **2020**, *790*, 139635. [CrossRef]
83. Jardim, P.M.; Solórzano, G.; Sande, J.B.V. Second phase formation in melt-spun Mg-Ca-Zn alloys. *Mater. Sci. Eng. A* **2004**, *381*, 196–205. [CrossRef]
84. Dutta, S.; Gupta, S.; Roy, M. Recent Developments in Magnesium Metal-Matrix Composites for Biomedical Applications: A Review. *ACS Biomater. Sci. Eng.* **2020**, *6*, 4748–4773. [CrossRef]
85. Bazhenov, V.; Koltygin, A.; Komissarov, A.; Li, A.; Bautin, V.; Khasenova, R.; Anishchenko, A.; Seferyan, A.; Komissarova, J.; Estrin, Y. Gallium-containing magnesium alloy for potential use as temporary implants in osteosynthesis. *J. Magnes. Alloy.* **2020**, *8*, 352–363. [CrossRef]
86. Bowen, P.K.; McNamara, C.T.; Mills, O.P.; Drelich, J.; Goldman, J. FIB-TEM Study of Magnesium Corrosion Products after 14 Days in the Murine Artery. *ACS Biomater. Sci. Eng.* **2015**, *1*, 919–926. [CrossRef] [PubMed]
87. Moritz, N.; Strandberg, N.; Zhao, D.S.; Mattila, R.; Paracchini, L.; Vallittu, P.K.; Aro, H.T. Mechanical properties and in vivo performance of load-bearing fiber-reinforced composite intramedullary nails with improved torsional strength. *J. Mech. Behav. Biomed. Mater.* **2014**, *40*, 127–139. [CrossRef] [PubMed]
88. ISO. ISO 10993-12:2012(en). In *Biological Evaluation of Medical Devices—Part 12: Sample Preparation and Reference Materials*; ISO: Geneva, Switzerland, 2012.
89. Gai, X.; Liu, C.; Wang, G.; Qin, Y.; Fan, C.; Liu, J.; Shi, Y. A novel method for evaluating the dynamic biocompatibility of degradable biomaterials based on real-time cell analysis. *Regen. Biomater.* **2020**, *7*, 321–329. [CrossRef]
90. Zhuang, Y.; Liu, Q.; Jia, G.; Li, H.; Yuan, G.; Yu, H. A Biomimetic Zinc Alloy Scaffold Coated with Brushite for Enhanced Cranial Bone Regeneration. *ACS Biomater. Sci. Eng.* **2020**. [CrossRef] [PubMed]
91. Guan, R.G.; Johnson, I.; Cui, T.; Zhao, T.; Zhao, Z.Y.; Li, X.; Liu, H. Electrodeposition of hydroxyapatite coating on Mg-4.0Zn-1.0Ca-0.6Zr alloy and in vitro evaluation of degradation, hemolysis, and cytotoxicity. *J. Biomed. Mater. Res.—Part A* **2012**, *100A*, 999–1015. [CrossRef] [PubMed]
92. Cahyono, N.A.; Sulistyani, L.D.; Santosa, A.S.; Latief, B.S. Analysis of the mechanical properties of magnesium equal-channel angular pressing of a plate on mandibular fracture through bending and ductility tests in physiological fluids of Dulbecco's Modified Eagle Medium. *J. Phys. Conf. Ser.* **2018**, *1073*, 062008. [CrossRef]
93. Mayama, T.; Tane, M.; Tadano, Y. Crystal plasticity analysis of anisotropic deformation behavior of porous magnesium with oriented pores. *J. Phys. Conf. Ser.* **2018**, *1063*, 012047. [CrossRef]
94. Fattah-alhosseini, A.; Chaharmahali, R.; Babaei, K. Effect of particles addition to solution of plasma electrolytic oxidation (PEO) on the properties of PEO coatings formed on magnesium and its alloys: A review. *J. Magnes. Alloy.* **2020**, *8*, 799–818. [CrossRef]
95. Mguni, L.L.; Mukenga, M.; Muzenda, E.; Jalama, K.; Meijboom, R. Expanding the synthesis of Stöber spheres: Towards the synthesis of nano-magnesium oxide and nano-zinc oxide. *J. Sol-Gel Sci. Technol.* **2013**, *66*, 91–99. [CrossRef]
96. De, A.K.; Mukhopadhyay, A.; Sen, S.; Puri, I.K. Numerical simulation of early stages of oxide formation in molten aluminium-magnesium alloys in a reverberatory furnace. *Model. Simul. Mater. Sci. Eng.* **2004**, *12*, 389–405. [CrossRef]
97. Gulbransen, E.A. The Oxidation and Evaporation of Magnesium at Temperatures from 400° to 500 °C. *Trans. Electrochem. Soc.* **1945**, *87*, 589–599. [CrossRef]
98. Ren, F.; Xin, R.; Ge, X.; Leng, Y. Characterization and structural analysis of zinc-substituted hydroxyapatites. *Acta Biomater.* **2009**, *5*, 3141–3149. [CrossRef] [PubMed]
99. LeGeros, R.Z.; LeGeros, J.P. Dense hydroxyapatite. An introduction to bioceramics. *World Sci.* **1993**, *1*.
100. Tripathy, A.P.N.K.; Patel, P.N. Preparation, IR, and lattice constant measurements of mixed (Ca+Cu+Zn) hydroxylapatites. *J. Solid State Chem.* **1989**, *80*, 1–5. [CrossRef]
101. Paul, S.; Ramasamy, P.; Das, M.; Mandal, D.; Renk, O.; Calin, M.; Eckert, J.; Bera, S. New Mg-Ca-Zn amorphous alloys: Biocompatibility, wettability and mechanical properties. *Materialia* **2020**, *12*, 100799. [CrossRef]
102. Fazel Anvari-Yazdi, A.; Tahermanesh, K.; Hadavi, S.M.; Talaei-Khozani, T.; Razmkhah, M.; Abed, S.M.; Mohtasebi, M.S. Cytotoxicity assessment of adipose-derived mesenchymal stem cells on synthesized biodegradable Mg-Zn-Ca alloys. *Mater. Sci. Eng. C* **2016**, *69*, 584–597. [CrossRef]
103. Zhang, C.; Lin, J.; Nguyen, N.T.; Guo, Y.; Xu, C.; Seo, C.; Villafana, E.; Jimenez, H.; Chai, Y.; Guan, R. Antimicrobial Bioresorbable Mg-Zn-Ca Alloy for Bone Repair in a Comparison Study with Mg-Zn-Sr Alloy and Pure Mg. *ACS Biomater. Sci. Eng.* **2020**, *6*, 517–538. [CrossRef]
104. Rahman, M.; Li, Y.; Wen, C. HA coating on Mg alloys for biomedical applications: A review. *J. Magnes. Alloy.* **2020**, *8*, 929–943. [CrossRef]
105. Zhang, H.; Zhao, C.; Wen, J.; Li, X.; Fu, L. Synthesis and structural characteristics of magnesium and zinc doped hydroxyapatite whiskers. *Ceram.—Silikaty* **2017**, *61*, 244–249. [CrossRef]
106. Rahim, M.I.; Babbar, A.; Lienenklaus, S.; Pils, M.C.; Rohde, M. Degradable magnesium implant-associated infections by bacterial biofilms induce robust localized and systemic inflammatory reactions in a mouse model. *Biomed. Mater.* **2017**, *12*, 055006. [CrossRef]

107. Willumeit-Römer, R. The Interface Between Degradable Mg and Tissue. *JOM* **2019**, *71*, 1447–1455. [CrossRef]
108. Cicha, I.; Singh, R.; Garlichs, C.D.; Alexiou, C. Nano-biomaterials for cardiovascular applications: Clinical perspective. *J. Control. Release* **2016**, *229*, 23–36. [CrossRef] [PubMed]
109. Dasgupta, S.; Banerjee, S.S.; Bandyopadhyay, A.; Bose, S. Zn- and Mg-doped hydroxyapatite nanoparticles for controlled release of protein. *Langmuir* **2010**, *26*, 4958–4964. [CrossRef]
110. Nassif, N.; Ghayad, I. Corrosion protection and surface treatment of magnesium alloys used for orthopedic applications. *Adv. Mater. Sci. Eng.* **2013**, *2013*. [CrossRef]
111. Rueda, L.M.; Nieves, C.; Barrios, C.A.H.; Coy, A.E.; Viejo, F. Design of TEOS-GPTMS sol-gel coatings on rare-earth magnesium alloys employed in the manufacture of orthopaedic implants. *J. Phys. Conf. Ser.* **2016**, *687*, 012013. [CrossRef]
112. Duan, X.W.; Liu, J.J.; Liu, L.L.; Gong, B.; Li, P.; Liu, B.S. Study on Constitutive Model and Dynamic Recrystallization Softening Behavior of AZ80A Magnesium Alloy. *Mater. Res. Express.* **2017**, *6*, 126576. [CrossRef]
113. Gummow, R.J.; He, Y. Morphology and Preferred Orientation of Pulse Electrodeposited Magnesium. *J. Electrochem. Soc.* **2010**, *157*, E45–E49. [CrossRef]
114. Yan, J.; Qin, Z.; Yan, K. Mechanical properties and microstructure evolution of Mg-6 wt% Zn alloy during equal-channel angular pressing. *Metals* **2018**, *8*, 841. [CrossRef]
115. Tong, X.; Wu, G.; Zhang, L.; Wang, Y.; Liu, W.; Ding, W. Microstructure and mechanical properties of repair welds of low-pressure sand-cast Mg–Y–RE–Zr alloy by tungsten inert gas welding. *J. Magnes. Alloy.* **2020**. [CrossRef]
116. Yao, X.; Tang, J.; Zhou, Y.; Atrens, A.; Dargusch, M.S.; Wiese, B.; Ebel, T.; Yan, M. Surface modification of biomedical Mg-Ca and Mg-Zn-Ca alloys using selective laser melting: Corrosion behaviour, microhardness and biocompatibility. *J. Magnes. Alloy.* **2020**. [CrossRef]
117. Chen, J.; Feng, J.; Yan, L.; Li, H.; Xiong, C.; Ma, S. In situ growth process of Mg–Fe layered double hydroxide conversion film on MgCa alloy. *J. Magnes. Alloy.* **2020**. [CrossRef]
118. Meibom, A.; Cuif, J.-P.; Hillion, F.; Constantz, B.R.; Juillet-Leclerc, A.; Dauphin, Y.; Watanabe, T.; Dunbar, R.B. Distribution of magnesium in coral skeleton. *Geophys. Res. Lett.* **2017**, *31*. [CrossRef]
119. Krishnan, K. Effect of microstructures and textures on the anisotropy of mechanical properties of AZ31 magnesium alloy sheets subjected to high strain rate rolling. *J. Phys. D Appl. Phys.* **2019**, in press.
120. Lee, J.; Lee, Y.-S.; Lee, M.-G.; Kim, D. Constitutive modelling of magnesium alloy sheets under strain path changes. *J. Phys. Conf. Ser.* **2016**, *734*, 032135. [CrossRef]
121. Sułkowski, B.; Janoska, M.; Boczkal, G.; Chulist, R.; Mroczkowski, M.; Pałka, P. The effect of severe plastic deformation on the Mg properties after CEC deformation. *J. Magnes. Alloy.* **2020**, *8*, 761–768. [CrossRef]
122. Atrens, A.; Liu, M.; Abidin, N.I.Z. Corrosion mechanism applicable to biodegradable magnesium implants. *Mater. Sci. Eng. B Solid-State Mater. Adv. Technol.* **2011**, *176*, 1609–1636. [CrossRef]
123. An, L.; Ma, Y.; Sun, L.; Wang, Z.; Wang, S. Investigation of mutual effects among additives in electrolyte for plasma electrolytic oxidation on magnesium alloys. *J. Magnes. Alloy.* **2020**, *8*, 523–536. [CrossRef]
124. Cesarz-Andraczke, K.; Nowosielski, R. Surface Structure and Corrosion Behavior of Mg 68−x Zn 28+x Ca 4 (x = 0.4) Bulk Metallic Glasses after Immersion in Ringer's Solution. *J. Mater. Eng. Perform.* **2019**, *28*, 2365–2377. [CrossRef]
125. Langelier, B.; Wang, X.; Esmaeili, S. Evolution of precipitation during non-isothermal ageing of an Mg-Ca-Zn alloy with high Ca content. *Mater. Sci. Eng. A* **2012**, *538*, 246–251. [CrossRef]
126. Wang, X.; Du, W.; Wang, Z.; Liu, K.; Li, S. Stable icosahedral phase in Mg44Zn44Gd12 alloy. *J. Rare Earths* **2012**, *30*, 503–506. [CrossRef]
127. Li, D.J.; Zeng, X.Q.; Dong, J.; Zhai, C.Q.; Ding, W.J. Microstructure evolution of Mg-10Gd-3Y-1.2Zn-0.4Zr alloy during heat-treatment at 773 K. *J. Alloys Compd.* **2009**, *468*, 164–169. [CrossRef]
128. Damodaran, V.B.; Murthy, S.N. Bio-inspired strategies for designing antifouling biomaterials. *Biomater. Res.* **2016**, *20*, 1–11. [CrossRef] [PubMed]
129. Li, X.; Filek, R.; Zhu, X.; Gao, H.; Qiao, L.; Liu, H.; Xie, L.; Wang, Y.; Pan, F.; Hutnik, C.M.L. Bio-modulation of scaring Glaucoma Filtration Surgery using a novel application of coated magnesium. *J. Magnes. Alloy.* **2020**. [CrossRef]
130. Gungor, A.; Incesu, A. Effects of alloying elements and thermomechanical process on the mechanical and corrosion properties of biodegradable Mg alloys. *J. Magnes. Alloy.* **2020**. [CrossRef]
131. Chaharmahali, R.; Fattah-alhosseini, A.; Babaei, K. Surface characterization and corrosion behavior of calcium phosphate (Ca-P) base composite layer on Mg and its alloys using plasma electrolytic oxidation (PEO): A review. *J. Magnes. Alloy.* **2020**. [CrossRef]
132. Yang, H.; Qu, X.; Lin, W.; Chen, D.; Zhu, D.; Dai, K.; Zheng, Y. Enhanced Osseointegration of Zn-Mg Composites by Tuning the Release of Zn Ions with Sacrificial Mg-Rich Anode Design. *ACS Biomater. Sci. Eng.* **2019**, *5*, 453–467. [CrossRef]
133. Yang, H.; Jia, B.; Zhang, Z.; Qu, X.; Li, G.; Lin, W.; Zhu, D.; Dai, K.; Zheng, Y. Alloying design of biodegradable zinc as promising bone implants for load-bearing applications. *Nat. Commun.* **2020**, *11*, 1–16. [CrossRef]
134. Tie, D.; Guan, R.; Liu, H.; Cipriano, A.; Liu, Y.; Wang, Q.; Huang, Y.; Hort, N. An in vivo study on the metabolism and osteogenic activity of bioabsorbable Mg-1Sr alloy. *Acta Biomater.* **2016**, *29*, 455–467. [CrossRef]

135. Lu, Y.; Wang, H.; Liu, J.; Ouyang, L.; Zhu, M. Destabilizing the dehydriding thermodynamics of MgH2 by reversible intermetallics formation in Mg−Ag−Zn ternary alloys. *J. Power Sources* **2018**, *396*, 796–802. [CrossRef]
136. Wasiur-Rahman, S.; Medraj, M. Critical assessment and thermodynamic modeling of the binary Mg-Zn, Ca-Zn and ternary Mg-Ca-Zn systems. *Intermetallics* **2009**, *17*, 847–864. [CrossRef]
137. Liao, H.; Kim, J.; Lee, T.; Song, J.; Peng, J.; Jiang, B.; Pan, F. Effect of heat treatment on LPSO morphology and mechanical properties of Mg–Zn–Y–Gd alloys. *J. Magnes. Alloy.* **2020**, 4–11. [CrossRef]